Journal of Volcanology and Geothermal Research 343 (2017) 155–170

Contents lists available at ScienceDirect

Journal of Volcanology and Geothermal Research

journal homepage: www.elsevier.com/locate/jvolgeores

Invited review article

# Bubble nucleation in magmas: A dominantly heterogeneous process?

Thomas Shea

*Department of Geology and Geophysics, University of Hawaii at Manoa, Honolulu, HI, 96822, United States*

ARTICLE INFO

*Article history:*
Received 30 April 2017
Received in revised form 22 June 2017
Accepted 29 June 2017
Available online 2 July 2017

ABSTRACT

Bubble nucleation is at the heart of magma ascent and degassing. Nucleation kinetics control how easily a magma exsolves its volatiles, and thereby its explosivity close to the surface. Homogeneous nucleation (i.e. without assistance from crystal substrates or other phases) often requires attainment of large supersaturation pressures ($\Delta P_N$ > 100 MPa, the change in pressure required for onset of nucleation), while heterogeneous nucleation on pre-existing crystals can occur at significantly lower values ($\Delta P_N$ < 50 MPa). Experiments have shown that both nucleation mechanisms are viable in the laboratory. The extent, however, to which one or the other nucleation mechanism dominates in nature is still unresolved. Yet, this distinction is fundamental for applications that employ nucleation theory and its derivatives. The classical nucleation theory allows calculations of nucleation rates in silicate melts, or conversely, yields valuable estimates of supersaturation pressures $\Delta P_N$ given experimental constraints on pressure conditions at the onset of nucleation. Decompression-rate meters (e.g. Toramaru, 2006) also relate the number density of bubbles in pyroclasts – a readily obtained textural characteristic – to rates of pressure change ($dP/dt$) during ascent. All these treatments require an explicit or implicit decision as to whether magma degassing was dominated by homogeneous or heterogeneous nucleation, which is guided by the choice of surface tension values. This contribution exploits the current textural datasets available for eruptions involving a variety of magma compositions to test the assumptions that homogeneous and/or heterogeneous nucleation dominate bubble vesiculation in natural melts. The comparison between pyroclast textures and those obtained via decompression experiments in the laboratory indicates that supersaturation pressures and decompression rates required for homogeneous nucleation are unrealistically high for natural magmas. I review the arguments for and against homogenous nucleation, and defend the alternate view that heterogeneous nucleation may dominate in all magma types, including rhyolites. In order to solve this central debate, our focus needs to be shifted towards understanding the pre-decompression phase equilibria and textural characteristics of magnetite in addition to the state of the melt structure.



**Contents**



*E-mail address:* tshea@hawaii.edu.

http://dx.doi.org/10.1016/j.jvolgeores.2017.06.025
0377-0273/

## 1. Background on bubble nucleation in silicate melts

Volatile exsolution is perhaps the most important phase transformation occurring in silicate melts as they migrate towards the surface. As volatiles (particularly $H_2O$, $CO_2$, $SO_4$) are converted into a separate vapor phase, they greatly enhance the capacity for magma ascent towards the surface by imparting higher buoyancies, and their expansion can result in significant overpressure. Thus, the processes governing volatile exsolution and outgassing, and particularly the timing of initial vapor phase nucleation with respect to depth in the conduit, effectively dictate a magma's explosive potential. $H_2O$ is the most soluble and the last volatile component to exsolve in most melts, likely exerting the dominant control on magma explosivity near the surface (e.g. Sparks et al., 1997; Andujar and Scaillet, 2012). In fact, Plinian eruptions involving mafic (e.g. basalt, basaltic-andesite), or evolved (e.g. dacite, rhyolite, trachyte, phonolite) magmas are generally linked with high initial $H_2O$ content (e.g. Etna 122 BCE, Del Carlo and Pompilio, 2004; Fontana Masaya 60 ka, Wehrmann et al., 2006; Mount St Helens 1980 CE, Blundy et al., 2008; Quilotoa 1280 CE, Stewart and Castro, 2016; Vesuvius 79 CE, Cioni, 2000; Santorini 3.6 ka, Druitt et al., 2016).

Our understanding of the solubility and mobility of water in silicate melts has improved remarkably owing to extensive suites of experimental studies (e.g. Liu et al., 2005; Zhang et al., 2007; Zhang and Ni, 2010 and references therein). In parallel, series of laboratory vesiculation experiments performed using different magma compositions (*rhyolite*, e.g. Hurwitz and Navon, 1994; Mangan and Sisson, 2000; Mourtada-Bonnefoi and Laporte, 2004; *dacite*, e.g. Mangan et al., 2004, Gardner and Ketcham, 2011; *phonolite*, Larsen and Gardner, 2004, Larsen, 2008, Shea et al., 2010a; Marxer et al., 2015; *andesite*, e.g. Fiege et al., 2014; *basalt*, Pichavant et al., 2013, Le Gall and Pichavant, 2016a, 2016b) have shed light on the mechanics and kinetics of degassing. In these experiments, a decrease in pressure – the driving force for water exsolution – is achieved step-wise or continuously from an initial value ($\Delta P = P_{initial} - P$) at a given rate, leading to bubble nucleation, growth/expansion, and in some cases, coalescence and collapse.

Several important lessons were derived from these studies, which have direct bearing on the dynamics of explosive eruptions. I briefly review these points in the next sections, charting in each case some of our current shortcomings regarding bubble formation in magmas.

### 1.1. Starting is half the battle

Nucleation kinetics exert the dominant control on degassing efficiency in silicate melts. Experiments in which bubbles nucleate homogeneously often require attainment of large supersaturation pressures ($\Delta P_N$). Values of $\Delta P_N$ necessary to trigger homogeneous nucleation in rhyolite melts often exceed 100 MPa (Mangan and Sisson, 2000; Mourtada-Bonnefoi and Laporte, 1999, 2002; Hamada et al., 2010; Gonnermann and Gardner, 2013). Over the relatively short timescales of magma ascent from their storage region to the surface, satisfying such supersaturation pressures may cause delays in homogeneous bubble nucleation. When nucleation finally occurs, degassing may occur at higher rates compared to an equilibrium scenario, in turn enhancing magma explosivity (Mangan and Sisson, 2000) (Fig. 1). In comparison, heterogeneous nucleation on pre-existing crystals, particularly Fe-Ti oxides, can occur at significantly lower $\Delta P_N$ (often < 50 MPa) (Hurwitz and Navon, 1994; Mangan et al., 2004; Larsen, 2008; Shea et al., 2010a). As a result, magmas that promote heterogeneous nucleation better track volatile solubility and degas along a path that is closer to equilibrium (Fig. 1). Crystal-poor rhyolite has been regarded as the epitome of homogeneous bubble nucleation, disequilibrium degassing and heightened explosivity, while other less viscous magmas (dacite, phonolite, basalt) are thought to more often foster heterogeneous nucleation with lower departures from equilibrium (Mangan et al., 2004; Larsen and Gardner, 2004; Larsen, 2008).

### 1.2. Surface tension is the key to bubble nucleation

According to classical theory (e.g. Hirth et al., 1970), the nucleation rate $J$ for $H_2O$ bubbles in a melt is expressed as:

$$J = J_0 \exp\left(-\frac{16\pi\sigma^3}{3k_BT\left(P_B^* - P_M\right)^2}\phi\right) \quad (1)$$

where $J_0 = \frac{2{n_0}^2 D_{H_2O} V_{H_2O}}{a_0}\sqrt{\frac{\sigma}{k_BT}}$ is the pre-exponential factor, $n_0$ is the concentration of water molecules per volume melt, $D_{H_2O}$ is the diffusivity of $H_2O$ at the bubble-melt interface, $V_{H2O}$ is the volume of a water molecule in the melt, $a_0$ is the distance between water molecules in the melt, $\sigma$ is the melt-bubble interfacial energy (= surface tension for liquids, typically expressed in N m$^{-1}$) or the energy required to create and maintain an interface between the bubble and the melt, $k_B$ the Boltzmann constant, $T$ the temperature, $P_B^*$ the internal pressure of the bubble nucleus, $P_M$ the pressure in the surrounding melt, and $\phi$ a geometrical term that defines the nucleation mechanism:

$$\phi = \frac{(2 - \cos\theta)(1 + \cos\theta)^2}{4} \quad (2)$$

For homogeneous nucleation $\phi = 1$, and for heterogeneous nucleation $0 < \phi < 1$ (see Fig. 2). A number of parameters from the classical nucleation equation (Eq. (1)) are reasonably well constrained ($D_{H_2O}$, $T$, $n_0$, $a_0$, $V_{H2O}$, $P_B^*$, cf. Mourtada-Bonnefoi and Laporte, 2002; Cluzel et al., 2008; Gonnermann and Gardner, 2013) and the uncertainties associated are not overly important (Fig. 3). In stark contrast, surface tension is cubed and exponentiated in Eq. (1), and even minor uncertainties cause extreme variations in calculated $J$ values (e.g. Mangan and Sisson, 2005). Because surface tension is in practice difficult to measure, studies have generally resorted to two workarounds: (a) adopting surface tension values measured using a macroscopic version of the vapor-melt contact

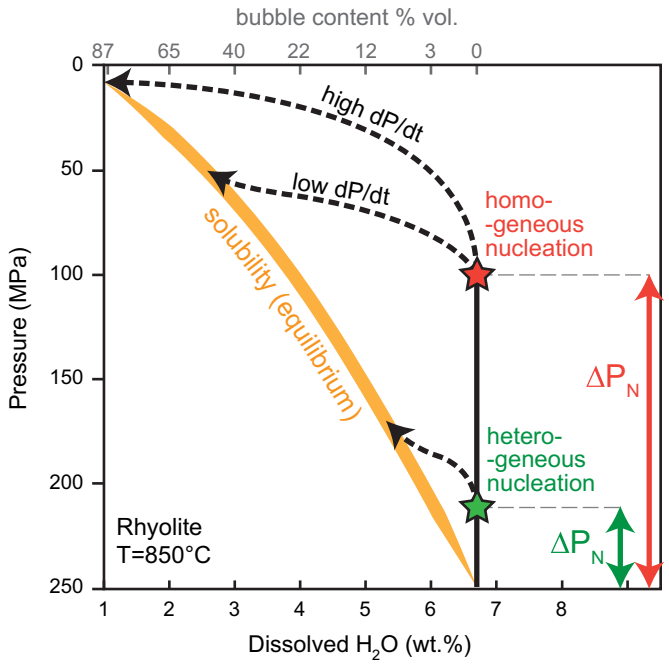


**Fig. 1.** The influence of nucleation behavior on degassing efficiency of a rhyolite melt (modified after Mangan and Sisson, 2000). Lower x-axis shows dissolved water content and upper x-axis the equivalent melt porosity. A water-saturated melt ascends from a storage region at ~250 MPa and either (1) starts to exsolve early via heterogeneous nucleation and tracks a near-equilibrium path defined by solubility (orange), or (2) exsolves late through homogeneous nucleation after attaining large values of supersaturation ($\Delta P_N$), in which case non-equilibrium degassing ensues. The extent of this departure from equilibrium will depend on the decompression rates.

(e.g. the sessile drop technique, Khitarov et al., 1979; Bagdassarov et al., 2000), in which case surface tension is labeled $\sigma^{\infty}$ to denote a large curvature radius compared to a critical nucleus (e.g. Gonnermann and Gardner, 2013), or (b) back-solving the classical nucleation equation for surface tension using nucleation rates calculated from laboratory experiments (Hurwitz and Navon, 1994; Mourtada-Bonnefoi and Laporte, 1999, 2002, 2004; Mangan and Sisson, 2000; Mangan and Sisson, 2005; Cluzel et al., 2008; Hamada et al., 2010; Shea et al., 2010a; Gardner and Ketcham, 2011; Gondé et al., 2011; Gardner et al., 2013; Fiege et al., 2014). Using the classical nucleation equation requires either homogeneous nucleation ($\phi = 1$ and a surface tension $\sigma_{hom}$), or heterogeneous nucleation to be assumed. In the latter case, the surface tension and $\phi$ are lumped into an effective surface tension term:

$$\sigma_{het} = \sigma_{hom}\phi^{1/3} \quad (3)$$

Note that $\sigma_{hom}$ may be obtained in this fashion if robust estimates of $\phi$ can be made by measuring the contact angle. In practice, however, contact angle measurements are difficult, and inevitably performed on the macroscopic bubble-crystal contact, yielding not $\sigma_{hom}$ but rather $\sigma^{\infty}$ (e.g. Hurwitz and Navon, 1994; Mangan and Sisson, 2005; Larsen, 2008). The geometric factor has also been calculated using the approximation $\Delta P_N^{het} / \Delta P_N^{hom} \approx \sqrt{\phi}$, where $\Delta P_N^{hom}$ and $\Delta P_N^{het}$ are the supersaturation pressures required for homogeneous and heterogeneous nucleation in a given set of experiments (Navon and Lyakhovsky, 1998). Existing estimates of contact angles increase in the order: feldspars (<20°, Hurwitz and Navon, 1994), pyroxenes (~40–60°, Larsen, 2008), hematite (~80–100°, Cluzel et al., 2008), magnetite (90–160°, Hurwitz and Navon, 1994; Mangan and Sisson, 2005) (Fig. 3b). The contact angle is also a function of crystal morphology, where sharp and acute crystal corners seem to reduce wetting of the melt on the mineral (Gardner and Denis, 2004; Cluzel et al., 2008). Clearly, Fe-Ti oxides, in particular magnetite/titanomagnetite (hereafter referred to as magnetite for simplification), are unrivaled in their ability to facilitate nucleation. Values of $\Delta P_N^{het}$ in magnetite-bearing experiments are as low as 15 MPa (Hurwitz and Navon, 1994), or 10 times less than values of $\Delta P_N^{hom}$ in similar rhyolite melts (e.g. Mourtada-Bonnefoi and Laporte, 2004).

Obtaining surface tension by solving the classical theory equation means that uncertainties in laboratory-derived experimental nucleation rates - and to a lesser extent $D_{H2O}$, $V_M$, $n_0$, and $P_B^*$ may all be compounded into a single "apparent" surface tension term (see Hammer, 2004 regarding the germane problem of deriving interfacial energy for crystal nucleation). Constraints on surface tension for homogeneous nucleation are currently most robust for rhyolite and dacite melts. Estimates of $\sigma^{\infty}$ from sessile drop measurements (Bagdassarov et al., 2000) under water saturated conditions span the range 0.07–0.15 N m$^{-1}$ and, in some cases, agree with $\sigma_{hom}$ calculated from decompression experiments (Gardner and Ketcham, 2011). In contrast, estimates of $\sigma_{het}$ suffer from a lack of physical measurements of contact angles, and are to date mostly inferred using Eq. (1) and experimental nucleation rates. Values of $\sigma_{het}$ were found to range between 0.025 and 0.08 N m$^{-1}$ (Gardner and Denis, 2004; Mangan and Sisson, 2005; Cluzel et al., 2008; Shea et al., 2010a), with the lowest values corresponding to magnetite-bearing experiments.

### *1.3. Pyroclast bubble textures can be used to infer magma decompression rates*

Toramaru (1989, 1995, 2006) developed a practical rate-meter guided by the classical nucleation theory that links the number density of bubbles per unit volume melt ($N_V$) in pyroclasts to rates of decompression ($dP/dt$) during ascent. The model was calibrated using decompression experiments, and has been used to extract decompression rates for a number of eruptions (e.g. Soufriere Hills 1997 CE, Giachetti et al., 2010; Vesuvius 79 CE, Shea et al., 2011; Chaiten 2008 CE, Alfano et al., 2012; Novarupta 1919 CE, Gonnermann and Houghton, 2012; Ruapehu 27 ka and 11 ka, Pardo et al., 2014; Etna 122 BCE and Green Tuff Pantelleria 46 ka, Campagnola et al., 2016). However, recent studies have identified some potential calibration issues with the Toramaru model (e.g. Fiege et al., 2014; Fiege and Cichy, 2015), but it is unclear to date whether these issues are inherent to the model or related to problems in the experimental studies used to test its reliability (or both). Popular user-friendly conduit flow software such as *Conflow* (Mastin and Ghiorso, 2000) have been recently modified to incorporate the decompression rate meter (*Confort15*, Campagnola et al., 2016), which will likely promote more widespread usage and rigorous testing.

The inferences gained from classical nucleation theory, experimental studies and applications to natural samples have significantly improved our knowledge of bubble nucleation kinetics, and highlight the potential for recovering essential eruption parameters such as decompression rates. However, applying our experimental knowledge to natural systems is not straightforward, typically because a decision must be made whether magma degassing was dominated by homogeneous or heterogeneous nucleation. Most often, this choice is made based on the presence/absence of Fe-Ti oxides, and their number density/abundance. Accordingly, natural samples, particularly those formed of rhyolite glass in which Fe-Ti oxides are not visually obvious or abundant enough in thin section, are often assumed to have undergone homogeneous nucleation or a combination of both homogeneous and heterogeneous nucleation.

The present study exploits the increasingly large number of textural datasets available for eruptions involving various magma compositions to test the assumptions that homogeneous and/or heterogeneous nucleation dominate bubble vesiculation and degassing in natural melts. The textural data is utilized as output constraints to calculate nucleation pressures via the classical nucleation theory, as well as decompression rates using the Toramaru model. The arguments in favor and against

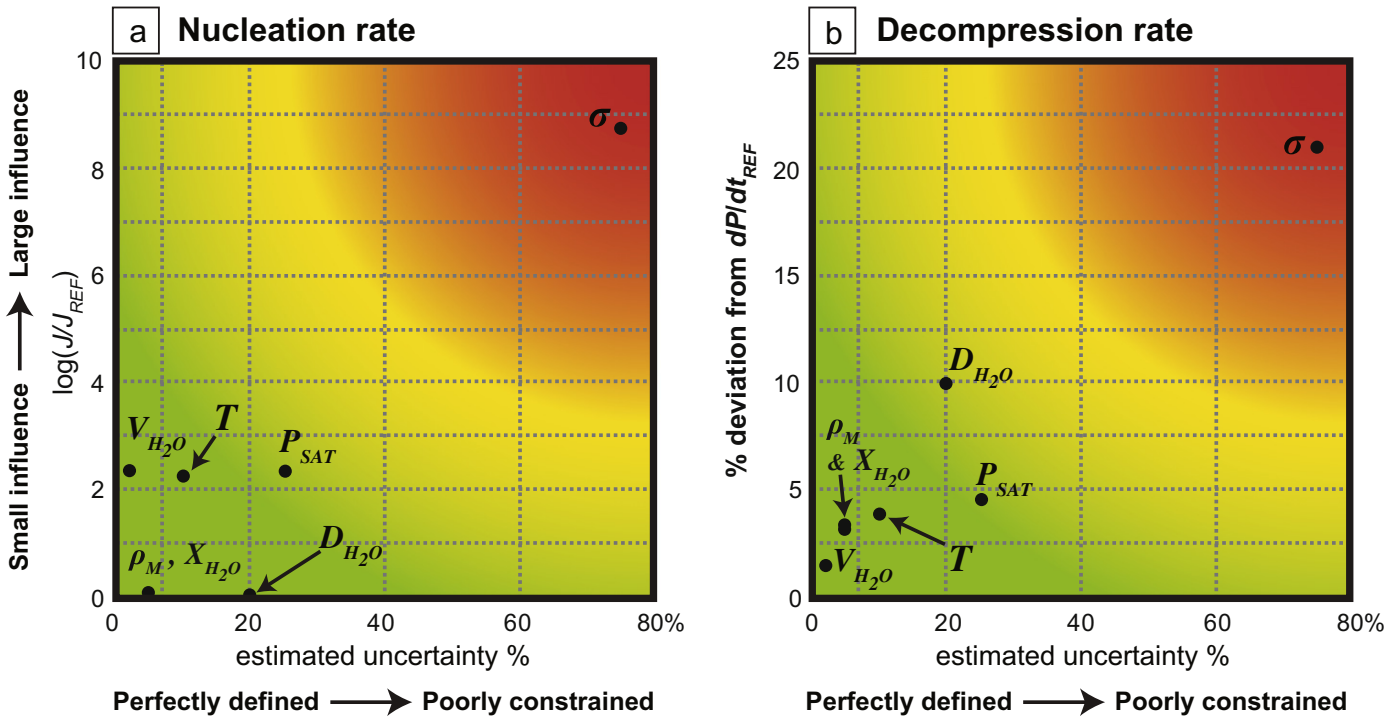


**Fig. 2.** "Influence" diagram for the main parameters involved in (a) nucleation and (b) decompression rate calculations using the classical nucleation theory (cf. Eq. (1)) and the Toramaru (2006) decompression rate meter (cf. Eq. (11)) respectively. The x-axis shows the estimated uncertainty as relative percentages, and the y-axis displays the influence of each variable on calculations of (a) nucleation rate (by dividing nucleation rate J, which is obtained after modifying a given variable by 10% of the reference value, by $J_{REF}$ the reference nucleation rate for the initial set of conditions*, and taking the log of the ratio) and (b) decompression rates (as percent deviation from the reference decompression rate $dP/dt_{REF}$). *Reference nucleation and decompression rates were calculated for a rhyolite melt assuming: initial pressure $P_{SAT} = 200$ MPa; melt temperature $T = 800$ °C; hydrous melt density $\rho_M = 2250$ kg m$^{-3}$; mole fraction water $X_{H2O} = 0.06$; volume of water molecules in melt $V_{H2O} = 3.48 \times 10^{-29}$ m$^{-3}$; bubble-melt surface tension $\sigma = 0.08$ N m$^{-1}$; and diffusivity of water $D_{H2O} = 5.2 \times 10$–$11$ m$^2$ s$^{-1}$.

different nucleation mechanisms are subsequently discussed, as I examine the potential implications for magma ascent and degassing.

## 2. Methods

### 2.1. Eruptions investigated

The choice of eruptions considered for this study was based on the availability of (1) storage and eruption parameters such as mass eruption rate (MER), erupted volume $V$, magma temperature $T$, initial pressure $P_{init}$ and $H_2O$ content, and (2) textural parameters derived from the study of pyroclasts, particularly bubble number densities $N_V$. Since the analytical resolution and methodology used to derive bubble number densities are critical to make robust comparisons, I chose mostly eruptions for which $N_V$ was calculated based on 2D image analysis (e.g. Shea et al., 2010b), which is still currently unrivaled for spatial resolution, relatively inexpensive, and less subject to post acquisition image treatments compared to 3D (e.g. Giachetti et al., 2011). In the rest of this article, bubble number densities values reported have typically been corrected for vesicle volume (and in some cases phenocryst

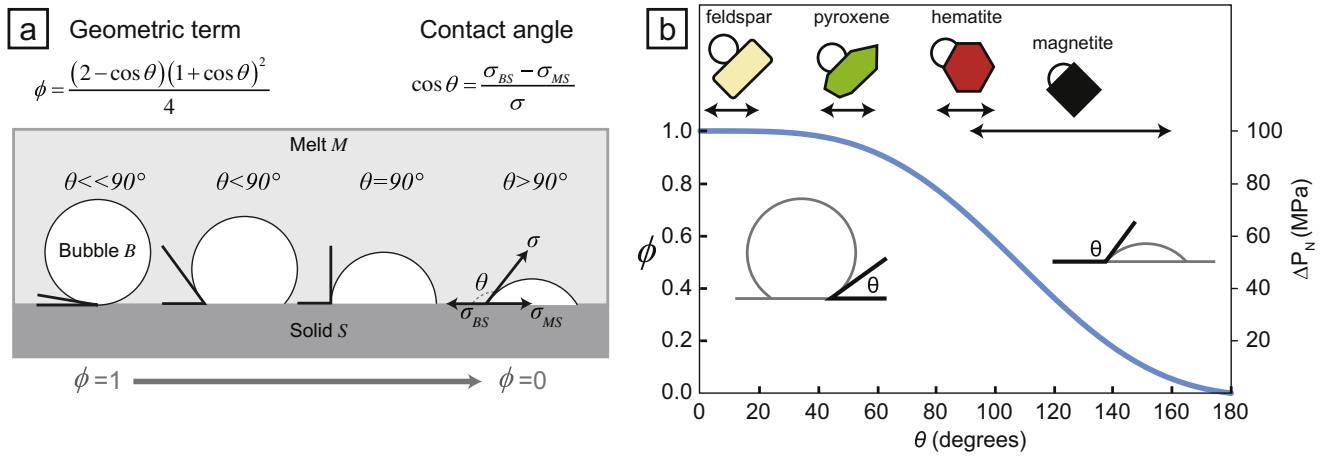


**Fig. 3.** The mechanics of heterogeneous nucleation. (a) The geometric term $\phi$ influences nucleation rate by reducing the surface tension term (cf. Eq. (1)). It depends entirely on the contact angle $\theta$ between the bubble interface and the solid (or more strictly the difference between the melt-solid and bubble-solid interfacial energies, $\sigma_{MS}$ and $\sigma_{BS}$). Higher angles are associated with poor wetting of the melt on the crystal, and reduce the energetic cost of nucleation ($\phi \to 0$ as $\theta \to 180°$). (b) Different minerals favor different bubble-crystal-melt contact angles. Feldspar is not considered an effective nucleation surface, while magnetite is the mineral least wetted by melt (i.e. with highest contact angle), drastically reducing the supersaturation pressure required for bubble nucleation (here taken for illustrative purposes to be equal to $\Delta P_N = 100$ MPa under the assumption of homogeneous nucleation conditions).

volume) in order to only account for their numeric abundance in the melt phase.

A total of 22 eruptions were found to meet the aforementioned selection criteria, and details on magma conditions and textural parameters can be found in the Supplementary material and in Table A1. The selection comprises eruptions involving:

- *Rhyolite melts* (n = 9): Askja 1875 CE (Iceland), Chaitén 2008 CE (Chile), Mt. Mazama 7.7 ka (USA), Mt. St. Helens 1980 CE (USA), Novarupta 1912 CE (USA), Mt. Pinatubo 1991 CE (Philippines), Quilotoa 1280 CE (Ecuador), Soufrière Hills 1997 CE (Montserrat), Taupo 181 CE (New Zealand). Note that while the bulk compositions of pyroclasts from several of these eruptions is andesitic or dacitic, the interstitial melt is always rhyolitic. Storage pressures vary from 60 to 260 MPa (~2.8–6.9 wt% $H_2O$ assuming water saturation conditions), magma temperatures from 780 to 1000 °C, and bubble number densities range between $N_V = 1.3 \times 10^5$ and $3 \times 10^6$ $mm^{-3}$. These eruptions encompass a variety of styles including Vulcanian, subplinian and Plinian.
- *Phonolitic-tephriphonolitic, and trachytic melts* (n = 4): Campanian Ignimbrite 39 ka (Italy), the Green Tuff 45 ka (Pantelleria), Mt. Vesuvius 79 CE and 512 CE (Italy), with storage pressures between 100 and 215 MPa, temperatures from 860 °C to 1200 °C, and $N_V = 0.2 \times 10^5$ and $1.5 \times 10^6$ $mm^{-3}$. These eruptions were subplinian to Plinian in style.
- *Basaltic and basaltic-andesitic melts* (n = 10): Villarica 2004 CE (Chile), Etna 122 BCE and Etna 2000 CE (Italy), Masaya Fontana 60 ka (Nicaragua), Kilauea Iki 1959 CE, Mauna Ulu 1969 CE, Pu'u 'O'o 1983–1986 CE fire fountaining and effusive activity (Hawaii), and Tarawera 1886 CE (New Zealand). Three of these eruptions attained Plinian intensities (Etna 122 BCE, Tarawera, and Fontana), and the rest typically vary between mild Strombolian to Hawaiian activity. Two factors complicate pre-eruption pressure ($P_{SAT}$) estimations for a number of these eruptions. (1) First, $CO_2$ in several instances (Etna 122 BCE, Kilauea Iki, Pu'u 'O'o) cannot be neglected, and modifies initial storage pressures recovered from melt inclusion or phase equilibria work (Wallace and Anderson, 1998; Del Carlo and Pompilio, 2004; Tuohy et al., 2016). The effects of $CO_2$ on bubble nucleation are not yet well established, and this problem is discussed further in the text. For these eruptions, it was assumed that bubble nucleation behavior is controlled by $H_2O$. (2) Second, some eruptions involve open-system conduits where magmas reside at shallow depths prior to eruption (e.g. Etna 2000 CE, Stromboli 2002 CE, Villarica 2004 CE). When these open-system magmas undergo decompression and fragmentation, they have already lost most of their initial $CO_2$, and have low water contents ($H_2O \leq$ 0.5 wt%. e.g. Witter et al., 2004; Métrich et al., 2010). For these eruptions, near surface, low initial pressures (1–10 MPa) were used in the nucleation models (see Table A1).

### 2.2. Supersaturation pressure and decompression rate calculations

#### 2.2.1. Calculation of supersaturation pressures

Supersaturation pressures $\Delta P_N = P_{SAT} - P_N$ required for the onset of nucleation (note: $P_N$ is nucleation pressure) were calculated using the classical nucleation theory (Eq. (1)). The parameters needed to obtain $J$ from the CNT (Eq. (1)) are detailed in this section.

During decompression, the internal pressure in the critical nucleus $P_B^*$ is not equal to the initial saturation pressure $P_{SAT}$, and can be calculated at any given melt pressure $P_L$ as (Cluzel et al., 2008):

$$\Gamma(P_B^*, T)P_B^* = \Gamma(P_{SAT}, T) \cdot P_{SAT} e^{\frac{V_{H_2O}}{kT}(P_L - P_{SAT})} \quad (4)$$

where $T$ is in Kelvins, $P$ in Pa/MPa, $\Gamma(P_{SAT},T)$ and $\Gamma(P_{SAT},T)$ are 'fugacity coefficients' that depend on pressure and temperature, and which can be calculated using programs like Loner14 (Bakker, 2003), or from the scripts given in the appendix of Holloway and Blank (1994) (provided here as the '*fugacity*' Matlab script in the Supplementary material).

The volume of a water molecule $V_{H_2O}$ ($m^{-3}$) is independent of silicate melt composition and can be calculated following Ochs and Lange (1999):

$$V_{H_2O} = 10^{-6} \times \frac{22.89 + 9.46 \times 10^{-3}(T - 726.85) - 3.15 \times 10^{-3}(P_M - 0.1)}{N_A} \quad (5)$$

where $T$ is melt temperature in Kelvins, $P_M$ melt pressure in MPa, and $N_A$ is the Avogadro number.

The number of initial water molecules per unit volume melt $n_0$ in Eq. (1) is:

$$n_0 = N_A X_{H_2O_T} \frac{\rho_M}{M_{H_2O}} \quad (6)$$

where $X_{H_2O_T}$ the mass fraction of $H_2O$ (molecular + hydroxyl) on a single oxygen basis (e.g. Zhang, 1999), $\rho_M$ the melt density (kg $m^{-3}$), and $M_{H2O}$ the molar mass of $H_2O$ (kg $mol^{-1}$). Rigorously, molecular ($X_{H_2O_m}$) and not total water ($X_{H_2O_T}$) should be used to derive $n_0$ (e.g. Mourtada-Bonnefoi and Laporte, 2004; Cluzel et al., 2008; Gardner and Ketcham, 2011; Preuss et al., 2016). This is, however, inconsequential to calculation of nucleation rates since higher $n_0$ values resulting from the use of $X_{H_2O_T}$ instead of $X_{H_2O_m}$ are largely counterbalanced by the necessity to replace faster diffusivity values for molecular water $D_{H_2O_m}$ by slower diffusivity of total water $D_{H_2O}$ in Eq. (1).

The average distance between water molecules in the melt $a_0$ (in m) is calculated from $n_0$:

$$a_0 = {n_0}^{-\frac{1}{3}} \quad (7)$$

The diffusivity term for total water $D_{H2O}$ varies as a function of magma composition, temperature, and $H_2O$ concentration (and therefore on pressure via solubility relationships). Water solubilities were calculated from the models of Liu et al. (2005) (rhyolite), Zhang et al. (2007) (dacite and basalt), and Di Matteo et al. (2004) (trachyte). For phonolite melts, I found that a modified form of the Liu et al. (2005) equation best reproduced the existing experimental data of Larsen (2008), Iacono Marziano et al. (2007), Carroll and Blank (1997), and Schmidt and Behrens (2008) for both Na and K phonolites:

$$C_{H_2O_T^{Phonolite}} = \frac{330{P_M}^{0.5} + 16P_M - 1.6{P_M}^{1.5}}{T} + 0.001{P_M}^{1.5} \quad (8)$$

where $C_{H_2O_T^{Phonolite}}$ is total water concentration (wt%), $P_M$ is in MPa and $T$ is in Kelvins.

Diffusivities were obtained using Ni and Zhang (2008), Ni et al. (2009), Zhang et al. (2007), Fanara et al. (2012), and Schmidt et al. (2013) for rhyolite, dacite, basalt, trachyte and phonolite melts respectively.

Equipped with estimates of surface tension (see Section 2.2.3), Eqs. (4)–(8) were used as inputs for Eq. (1) to obtain nucleation rates $J$ ($m^{-3}$ $s^{-1}$). Finally, to calculate $\Delta P_N$, the supersaturation pressure required for nucleation, bubble number densities were computed by integrating nucleation rate through all decompression steps:

$$N_{V(i)} = J_i t_i \quad (9)$$

where $t$ is decompression time (s) at step $i$ and for a pressure increment $\delta P$, and is expressed as (e.g. Mourtada-Bonnefoi and Laporte, 2004):

$$t_i = i \cdot \delta P \cdot \frac{dP}{dt} \quad (10)$$

The latter was used with Eq. (9) to obtain the cumulative bubble number density $N_V$ along the decompression path. For Eq. (10), an

arbitrary decompression rate of 0.1 MPa/s was chosen for all simulations. This choice has little influence on the supersaturation pressures calculated (Mourtada-Bonnefoi and Laporte, 2004). The supersaturation pressure required for nucleation $\Delta P_N$ can then be defined as the pressure $P_N$ at which $N_i \geq 1$ mm$^{-3}$, which can be considered a minimum bubble number density that could be resolved within an experimental charge or a thin section of a natural pyroclast (e.g. Cluzel et al., 2008). Changing this 'detection threshold' by a factor of 10 only modifies calculated supersaturation pressures by 1–2 MPa. Finally, the saturation pressure $P_{SAT}$ required to compute $\Delta P_N = P_{SAT} - P_N$ is a known parameter for the eruptions investigated here and the experimental data (cf. Table A1).

At this stage, it is worth emphasizing that the nucleation rates obtained using the CNT are solely used to (1) back-calculate surface tension for experiments where the nucleation pressure $P_N$ is known, and (2) estimate nucleation pressures of natural magmas given reasonable values of surface tension. Nucleation rates and bubble number densities calculated using the CNT are not utilized for one-to-one textural comparisons with experimental and natural samples because they vary significantly within very narrow pressure ranges, and also depend on bubble growth dynamics once nucleation rates reach a certain value (Toramaru, 1995). Here, calculations stop when bubble number densities attain the inferred detection limit for petrographic observation ($N_i = 1$ mm$^{-3}$). The effects of diffusive bubble growth on modulating nucleation rates by reducing volatile supersaturation (e.g. Gonnermann and Houghton, 2012) can effectively be neglected at such low bubble number densities. Indeed, decompression timescales required to increase $J$ by several orders of magnitude around $P_N$ are far shorter (order of seconds) than the timescales required for diffusion of water between bubbles at these low number densities (for a ~1 mm interbubble distance, diffusion times are in the order of minutes to hours for basalt and rhyolite at 800 °C and 1200 °C respectively, and 200 MPa). It should be noted that, if anything, reducing volatile supersaturation in the melt via bubble growth would require higher values of supersaturation pressure required to attain detectable $N_i$.

### 2.2.2. Calculation of decompression rates

The equation of Toramaru (2006) relates bubble number densities $N_V$ to decompression rate $dP/dt$ as follows:

$$N_V \approx 34 n_0 \left(\frac{16\pi\sigma^3}{3k_B T P_{SAT}^2}\right)^{-2} \left(\frac{V_{H_2O} P_{SAT}}{k_B T}\right)^{-1/4} \left(\frac{P_{SAT}^2 k_B T n_0 D_{H_2O}}{4\sigma^2 \left|dP/dt\right|}\right)^{-3/2} \quad (11)$$

The parameters used are the same as in Eq. (1). There is, however, a notable difference in the meaning of the diffusivity term $D_{H_2O}$. In the classical nucleation equation, the diffusivity term is sensu stricto the rate at which molecules can attach to the critical nucleus to form the interface, whereas in the Toramaru model, it has the meaning of bulk diffusivity in the melt. Although the two are approximated by the same term, on one hand it increases nucleation rates (Eq. (1)), while on the other it acts to decrease the number of bubbles nucleated (Eq. (11)). This is because the Toramaru model accounts for the fact that higher diffusivities favor migration of $H_2O$ into already existing neighboring bubbles, which is less energetically costly than forming new nucleii.

Values of $N_V$ from the available experimental data as well as the different eruptions examined were used as output constraints for decompression rates calculations. The saturation pressure $P_{SAT}$ is chosen to match the conditions inferred for each eruption (or those applied in experimental studies). Shea et al. (2011) argued that for eruptions where bubble nucleation was likely continuous during ascent (e.g., Vesuvius 79 CE), choosing pre-eruption storage pressure for $P_{SAT}$ in decompression rate calculations was not entirely realistic because the majority of the bubbles controlling $N_V$ values nucleate late during ascent (i.e. when pressures, $H_2O$ concentrations, and thereby diffusivities are all lower). The assumption that $P_{SAT}$ is the initial storage pressure is therefore more valid for eruptions where nucleation would have been delayed significantly, and high $H_2O$ maintained up to shallow levels (e.g. Mangan and Sisson, 2000). The inferred storage pressure was adopted as $P_{SAT}$ for all calculations despite these concerns, to (1) avoid circular reasoning by making inferences on how early or late degassing initiated during ascent, and (2) to maximize the potential for nucleation in cases where large (e.g. ≥100 MPa) supersaturation pressures might be required (e.g. Mourtada-Bonnefoi and Laporte, 2004). For each eruption, both homogeneous and heterogeneous nucleation assumptions were tested by using different values of surface tension (cf. next section).

### 2.2.3. Choice of surface tension values

The choice of surface tension values for both homogeneous and heterogeneous nucleation was guided by existing experimental data. The only physical measurements of surface tension under different conditions of $P_{H2O}$ and $T$ were made by Khitarov et al. (1979) and Bagdassarov et al. (2000) in basalt and rhyolite melt. The more extensive data of Bagdassarov et al. (2000) can be fitted by the empirical relation:

$$\sigma^{\infty} = 0.175 \cdot \exp(-0.0025 P_M) + 7.3 \times 10^{-5}(T - 1000) \quad (12)$$

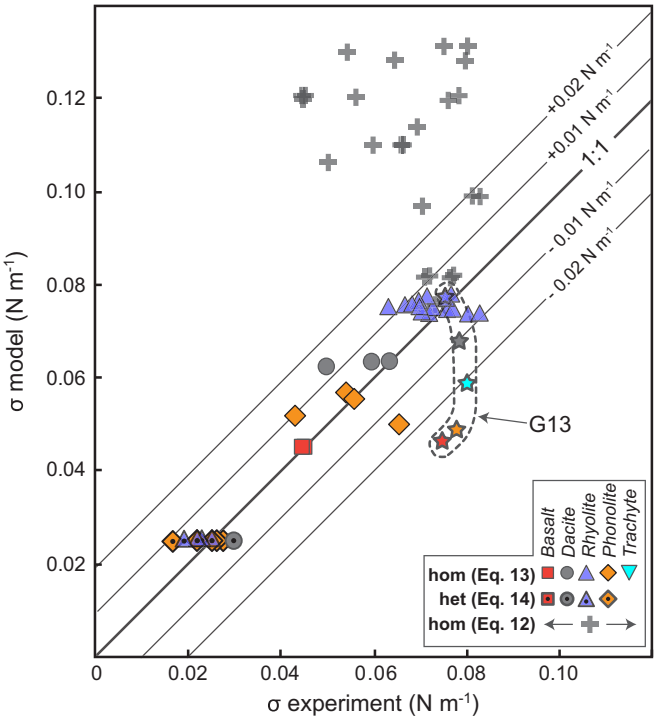


**Fig. 4.** Surface tension models tested in this contribution and their ability to reproduce experimental data. Values on the x-axis were calculated from experimental studies* by solving the classical nucleation theory (Eq. (1)) for supersaturation pressures required to initiate nucleation. Values on the y-axis are those calculated by an empirical model for macroscopic surface tension in rhyolite (crosses, Eq. (12)), a generic model for surface tension for homogeneous nucleation proposed in the text (colored symbols, Eq. (13)), and a constant value σhet = 0.025 N m$^{-1}$ (colored symbols with dot Eq. (14)). *Experimental data: rhyolite: Gardner et al. (1999); Mangan and Sisson (2000); Mourtada-Bonnefoi and Laporte (2004); Gardner and Denis (2004); Cluzel et al. (2008); Hamada et al. (2010); Gardner and Ketcham (2011); Gardner et al. (2013); Gonnermann and Gardner (2013). Dacite: Mangan et al. (2004); Mangan and Sisson (2005); Gardner and Ketcham (2011); Gardner et al. (2013). Basalt: Gardner et al., 2013; Le Gall and Pichavant, 2016a, 2016b. Phonolite: Larsen and Gardner (2004); Iacono Marziano et al. (2007); Larsen (2008); Shea et al. (2010a); Gardner (2012); Gardner et al., 2013; Marxer et al., 2015. Trachyte: Gardner et al. (2013).

with $P_M$ in MPa and $T$ in degrees Celsius. This form is slightly different from that of Bagdassarov et al. (2000) and provides a better fit to their $P_{H2O} > 0.1$ MPa experiments.

Other surface tension estimates are usually obtained by solving the classical nucleation theory (Eq. (1)) for an 'effective' value using the supersaturation pressure required for nucleation in decompression experiments, and/or using measured values of nucleation rate. Here, surface tension is calculated exclusively using supersaturation pressures observed within experiments, to avoid uncertainties inherent to nucleation rates and the choice of the time interval used for their derivation. Despite the abundance of surface tension estimates in the literature, they were entirely re-calculated for this work using the available experimental data, in order to avoid differences in the choice of parameter values (e.g. $D_{H_2O}$, $V_{H_2O}$, use of $P_B^*$ or $P_{SAT}$, etc.…). The datasets in which the supersaturation pressure required for nucleation is available (or can be inferred) are reported in Supplementary Table A1 (n = 18 studies). The resulting values of surface tension for experiments in which homogeneous nucleation is assumed range between 0.045 and 0.083 N m$^{-1}$, with lower values corresponding to basalts (e.g. Le Gall and Pichavant, 2016a, 2016b), and higher values to rhyolites (e.g. Mangan and Sisson, 2000). The values are lower in most cases than values that would be predicted from the pressure- and temperature-dependent empirical expression for $\sigma^{\infty}$ in rhyolite derived from Eq. (12), consistent with previous observations (e.g. Gonnermann and Gardner, 2013; Colucci et al., 2016) (Fig. 4). Although the present calculations confirm that effective surface tension may depend on melt composition (e.g. Mangan and Sisson, 2005; Gardner and Ketcham, 2011), it should be noted that a different study involving a wide range in compositions (basaltic-andesite, dacite, rhyolite, trachyte and phono-tephrite) found little resolvable compositional dependence (Gardner et al., 2013). For the present work, surface tension was parameterized as a function of $P_{H2O}$, $T$, and melt composition, to fit the values compiled from the different experimental datasets, taking the form:

$$\sigma^{hom} = \sigma_{ref} \times \exp\left[-2.2 \times 10^{-2} \times \left(SiO_{2_{ref}} - SiO_2\right)\right] - 5 \times 10^{-6}\left(T_{ref} - T\right) + 2 \times 10^{-5}\left(P_{ref} - P\right) \quad (13)$$

where $\sigma_{ref}$, $T_{ref}$, $P_{ref}$, $SiO_{2_{ref}}$ are the surface tension, temperature, pressure, and $SiO_2$ content of a reference melt chosen here to take values $\sigma_{ref} =$ 0.06 N m$^{-1}$, $T_{ref} = 900$ °C, $P_{ref} = 200$ MPa, $SiO_{2_{ref}} = 66.5$ wt%. This empirical fit reproduces the data with an average difference of 0.0042 N m$^{-1}$ if the Gardner et al. (2013) experiments are excluded, and of 0.0071 N m$^{-1}$ if they are included (Fig. 4). The two different expressions for surface tension for homogeneous nucleation (composition-independent and composition-dependent Eqs. (12) and (13) respectively) were tested in this contribution.

Surface tension for heterogeneous nucleation is strongly controlled by the phase on which bubbles nucleate (Hurwitz and Navon, 1994; Gardner and Denis, 2004; Mangan and Sisson, 2005; Cluzel et al., 2008). For the models presented here, I assume this phase is magnetite, consistent with observations made in natural samples (Sable et al., 2009; Giachetti et al., 2010; Shea et al., 2010a, 2012; Colombier et al., 2017). Values of surface tension for heterogeneous nucleation on Fe-Te oxides obtained here vary between 0.017 and 0.03 N m$^{-1}$, with no obvious dependence on melt composition. A single average value was therefore chosen for all melts:

$$\sigma^{het} = 0.025 \text{ N m}^{-1} \quad (14)$$

Results pertaining to calculations of supersaturation pressures and decompression rates that follow were thus derived using Eq. (12) or (13) for homogeneous nucleation, and Eq. (14) for heterogeneous nucleation.

## 3. Results

### 3.1. Supersaturation pressures for bubble nucleation

The amount of decompression required to trigger bubble nucleation is predictably much higher for all eruptions when homogeneous nucleation is assumed compared to the heterogeneous case ($\Delta P_N^{hom} \sim 40$–200 MPa and $\Delta P_N^{het} \sim 15$–30 MPa, Fig. 5). To assess whether these supersaturation pressures are realistic, the values are compared to initial pre-eruptive pressures inferred for each eruption. In a way, these magma storage pressures should represent the maximum possible pressure ranges through which nucleation could have occurred. Supersaturation pressures calculated using surface tension values $\sigma^{\infty}$ corresponding to macroscopic measurements that are not composition dependent (Eq. (12)) are in most cases larger than the initial storage pressures inferred for most eruptions ($\Delta P_N^{hom} = 180$–200 MPa). Values of $\Delta P_N^{hom}$ obtained from the composition-dependent expression (Eq. (13)) are comparatively lower (40–140 MPa), in several cases well below initial storage pressures inferred (Pinatubo 1991 CE, Mt. St Helens 1980 CE, Campanian Ignimbrite 39 ka, Etna 122 BCE, Vesuvius 79 CE), in other instances near or slightly below storage pressures (Chaiten 2008 CE, Taupo 181 CE, Crater Lake 7.7 ka, Quilotoa 1280 CE, Masaya 60 ka, Vesuvius 512 CE, Tarawera 1886 CE), with four eruptions yielding $\Delta P_N^{hom}$ equal to or above pre-eruptive pressures (Askja 1875 CE, Soufriere Hills 1997 CE, Novarupta 1912 CE, Pantelleria 45 ka). Because $\sigma^{hom}$ depends on melt composition when Eq. (13) is used, supersaturation pressures for homogeneous nucleation follow the sequence $\Delta P_N^{hom/rhyolite} > \Delta P_N^{hom/trachyte} \geq \Delta P_N^{hom/phonolite} > \Delta P_N^{hom/basalt}$.

In contrast, supersaturation pressures are invariably much lower than inferred pre-eruptive storage pressures under the heterogeneous nucleation assumption, typically accounting for 15–34% of the total allowable pressure (e.g. $\Delta P_N^{het} = 38$ MPa for Mt. St Helens 1980 CE with an initial storage $P_{SAT} \sim 255$ MPa, or $\Delta P_N^{het} = 17$ MPa for Fontana Lapilli 60 ka with pressure $P_{SAT} \sim 50$ MPa).

### 3.2. Magma decompression rates

#### 3.2.1. How well does the Toramaru model perform?

Recent studies have identified some potential calibration issues with the Toramaru model (e.g. Fiege et al., 2014; Fiege and Cichy, 2015). Therefore, before applying the decompression rate meter to the eruptions selected here, the model was tested against existing experimental data for decompression of $H_2O$-saturated rhyolite, dacite, phonolite and basalt melts. The decompression rates imposed during the experiments were compared with values obtained using the Toramaru (2006) model using surface tension values obtained by solving Eq. (1) for supersaturation pressures (see Section 2.2.3). Experimental data available for basaltic compositions is currently sparse, and only the $H_2O$-saturated runs of Le Gall and Pichavant (2016a, 2016b) and Gardner et al. (2013) were included here.

Different decompression protocols have been used in experimental vesiculation studies. Single-step decompression approaches (SSD; e.g. Hurwitz and Navon, 1994; Mourtada-Bonnefoi and Laporte, 1999; Gardner and Denis, 2004; Gardner and Ketcham, 2011; Gardner et al., 2013) usually submit the charge to one short pressure drop, and quench the experiment after different dwell times at the final conditions. In multi-step (MSD; Larsen, 2008, Shea et al., 2010a, Cichy et al., 2011) and continuous (CD; Mangan and Sisson, 2000; Mourtada-Bonnefoi and Laporte, 2004; Mangan et al., 2004; Cluzel et al., 2008; Hamada et al., 2010; Fiege et al., 2014) decompression experiments, the runs are usually quenched as 'snapshots' at different final pressures. Each technique has its own sets of pros and cons, which are discussed elsewhere (e.g. Nowak et al., 2011; Marxer et al., 2015; Fiege and Cichy, 2015). Several types of starting materials are also used for decompression experiments: crushed/powdered glass or whole cylinders (c.f. Preuss et al., 2016), and some prefer superfused (i.e. melts brought to temperatures

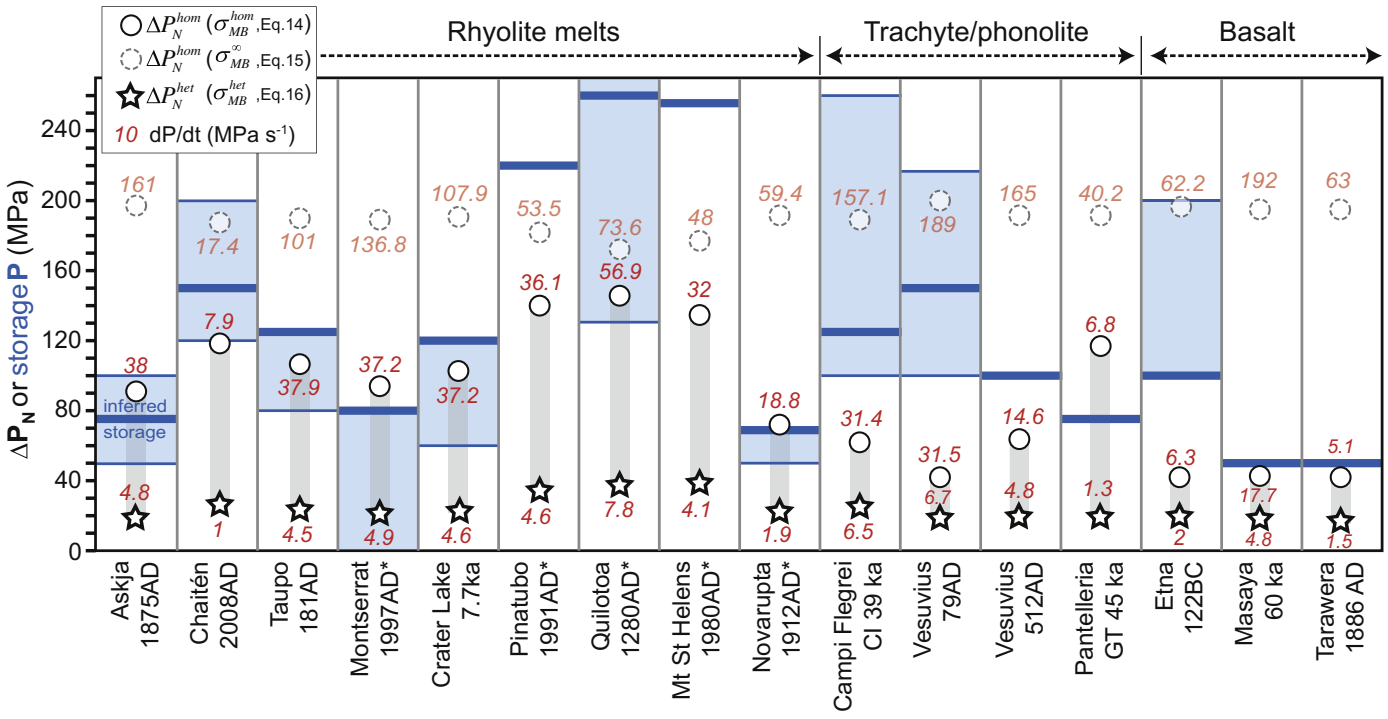


**Fig. 5.** Supersaturation pressures required to trigger homogeneous ($\Delta P_N^{hom}$) and heterogeneous ($\Delta P_N^{het}$) nucleation for highly explosive (i.e. Vulcanian, sub-Plinian and Plinian) eruptions involving magmas of various compositions (see Table A1 for details). For each eruption, the inferred storage pressure is shown as a thick blue line (preferred value) with thin blue lines representing the range from the literature. Supersaturation pressures (round and star symbols), and decompression rates (in red, MPa/s) are calculated using Eqs. (1) and (11) respectively, assuming either surface tension for homogeneous (Eq. (13)) or for heterogeneous (Eq. (14)) nucleation. When multiple eruptive phases are available for a given eruption, decompression rates are the average of all phases. Decompression rates and $\Delta P_N^{hom}$ values were also calculated using 'macroscopic' values of surface tensions calculated using Eq. (12) (dotted circles).

well over the liquidus) starting material to render the charge initially more homogeneous, while others choose starting melts that have not undergone superliquidus treatments. The latter choice is likely important as superliquidus treatments are known to affect the pre-decompression melt structure (e.g. Hammer, 2008 and references therein). Finally, experimental charges go through different textural characterization techniques, from measurements of 2D sections under the microscope or SEM with or without stereological conversions (Hurwitz and Navon, 1994; Larsen and Gardner, 2004; Shea et al., 2010b), to 3D characterization using x-ray tomography renderings (Gardner and Ketcham, 2011; Nowak et al., 2011; Le Gall and Pichavant, 2016a, 2016b). Clearly, a more rigorous test of the Toramaru model would ideally compare series of decompression experiments performed in the same laboratory with the same protocol for preparing the starting material, for decompression, and for characterizing bubble number densities. The use of a single value for surface tension $\sigma^{het} = 0.025$ N m$^{-1}$ for heterogeneous nucleation on magnetite independent of pressure and temperature effects or melt composition is also a simplification. Therefore, at present, the available experimental data can only provide a first order indication of how successful the model is at reproducing decompression rates from BNDs.

Considering the numerous aforementioned sources of uncertainties, the current compilation shows a fairly good correspondence between calculated decompression rates from Eq. (11) and those imposed in experiments (Fig. 6). Experiments performed using single-step decompression approaches correlate poorly with the Toramaru model, whereas continuous and multi-step decompression procedures typically yield better matches (Fig. 6a). If SSD runs are excluded, the model performs best in the case of rhyolite, with most of the experimental decompression rates reproduced within a factor of ~3, while there is significantly more scatter for melts of other compositions (Fig. 6b). There is no obvious indication that overestimates are more frequent than underestimates. As a whole, these results show that despite the significant uncertainty inherent to the experimental data available, decompression rates appear to be reasonably well estimated by the Toramaru (2006) model.

### 3.2.2. Decompression rates of natural magmas

The decompression path of magmas towards the surface is likely non-linear (e.g., Neri et al., 2002; Su and Huber, 2017); therefore, decompression rates calculated using total bubble number density will likely represent a near-maximum value attained during the eruption phase in which the pyroclasts were sampled (e.g. Shea et al., 2011).

Decompression rates calculated under the assumption of homogeneous nucleation with composition-dependent surface tension (Eq. (13)) vary between 5 and 57 MPa/s, and between 17 and 192 MPa/s using composition-independent surface tension values (Eq. (12)) (Fig. 5). Rates are much lower under the assumption of heterogeneous nucleation, with a range 1–7.8 MPa/s. There are no obvious differences in $dP/dt$ between magmas of different compositions for eruptions of comparable intensities (e.g. Plinian eruptions such as Fontana 60 ka, Vesuvius 79 CE, Campanian Ignimbrite 39 ka, or Novarupta 1912 CE).

Independent estimates of decompression rates relevant to explosive eruptions vary considerably (e.g. Rutherford, 2008 for a review) (Fig. 7). Rates inferred by comparing microlite textures with those derived from kinetic experiments range from ~0.0001–1.4 MPa/s (e.g. Geschwind and Rutherford, 1995; Couch et al., 2003; Castro and Gardner, 2008; Andrews, 2014; Szramek, 2016), similar to values obtained using diffusion rates of volatiles in melt embayments (0.001–1.6 MPa/s, Liu et al., 2007; Humphreys et al., 2008; Lloyd et al., 2014; Ferguson et al., 2016; Myers et al., 2016) and from modeling phenocryst breakage during ascent and vesiculation (Miwa and Geshi, 2012). Amphibole breakdown rims that form during magma decompression give slightly lower decompression rates (~0.0005–0.1 MPa/s, Rutherford and Hill, 1993; Rutherford and Devine, 2003; Nicholis and Rutherford, 2004). Conduit ascent and magma degassing models require higher decompression rates (0.01–10 MPa/s) to adequately reproduce magma discharge

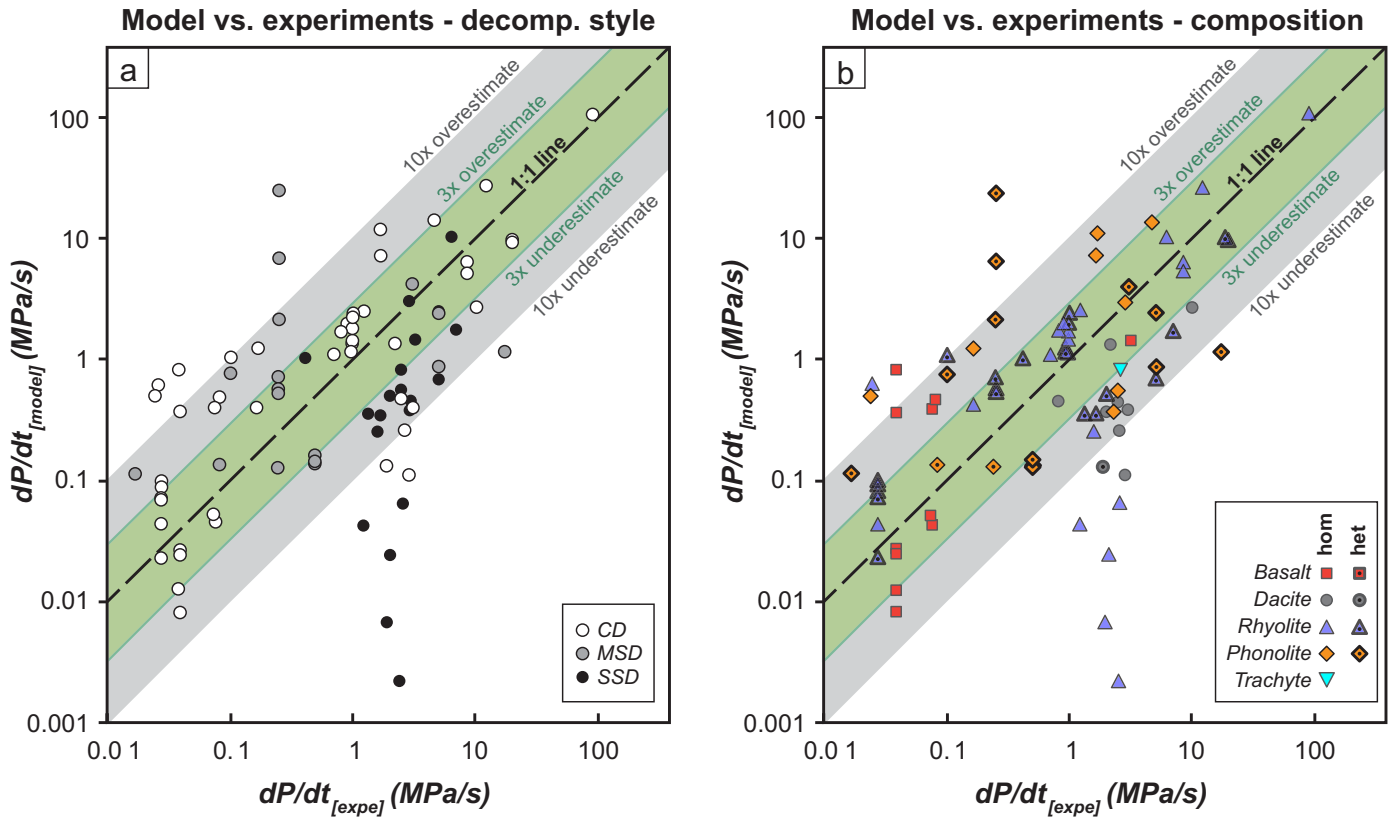


**Fig. 6.** Comparisons between decompression rates imposed in laboratory experiments and those calculated via the Toramaru (2006) model using measured bubble number densities. (a) Data distinguished by decompression style (CD, MSD, SSD for continuous, multi-step, and single-step decompression respectively) illustrating that SSD experiments are likely not well suited for this comparison. (b) Data separated by melt composition and inferred nucleation mechanism (homogeneous vs. heterogeneous). If SSD data is excluded, rhyolite experiments are typically well reproduced by the model, while other compositions show more scatter. There is no obvious correlation between how well the model does and the inferred nucleation mechanism.

rates or pumice textures at the fragmentation level relevant to highly explosive eruptions (e.g. Papale and Dobran, 1993; Kaminski and Jaupart, 1997; Papale et al., 1998) (Fig. 7). The maximum decompression rates calculated via bubble number densities herein compare best with estimates from physical/numerical models, but only if nucleation is heterogeneous. Assuming homogeneous nucleation yields rates that are typically >10 MPa/s (Fig. 5), higher than any independent estimates from petrological, textural or modeling observations.

## 4. Discussion

This section first revisits the reasoning behind the common assumption that most crystal-poor magmas undergo homogeneous nucleation, underscoring that our arguments largely rely on the absence of magnetite. I then emphasize the strong possibility that the melt structure itself can play an important role in modifying nucleation behavior in experiments and in natural magma. The interpretation and use of the main textural characteristic resulting from the nucleation process (bubble number density) to recover key physical eruption parameters is subsequently discussed in light of the results presented above. Finally, I outline that highly explosive eruptions may not be necessarily synonymous with extreme levels of supersaturation and non-equilibrium degassing, and can just as well be fueled by magmas that undergo heterogeneous nucleation.

### *4.1. Arguments for and against homogeneous bubble nucleation: all about magnetite?*

The importance of assuming homogeneous or heterogeneous bubble nucleation in the context of magma degassing cannot be overstated. The above results confirm previous inferences (e.g. Hurwitz and Navon, 1994; Cluzel et al., 2008; Fiege and Cichy, 2015) that the value adopted for surface tension exerts the major control on both supersaturation pressures needed for nucleation and decompression rates obtained from the number of bubbles that nucleated. Since $\Delta P_N$ and $dP/dt$ govern the degassing style (equilibrium vs. non-equilibrium) and explosivity of magmas towards the surface, it is essential to revisit in detail the rationale for favoring homogeneous over heterogeneous nucleation.

By far the most widespread lines of reasoning in favor of homogeneous nucleation are (1) a visible lack of obvious microlites as nucleation sites, or (2) not enough of them to match bubble number densities and therefore control nucleation. These arguments have been used in the context of dacitic and rhyolitic eruptions because the pyroclasts produced are typically microlite-poor (Klug et al., 2002; Adams et al., 2006; Bouvet de Maisonneuve et al., 2009; Carey et al., 2009; Houghton et al., 2010; Gondé et al., 2011; Alfano et al., 2012; Gonnermann and Houghton, 2012), as well as for scoria from basaltic Plinian eruptions (e.g. Costantini et al., 2010). In the framework of bubble nucleation, most microlite phases present within eruptions products (e.g. plagioclase, Na-K feldspar, clino/orthopyroxene, amphibole, olivine, feldspathoids) are unlikely to provide very efficient sites to lower interfacial energy (Fig. 3). Therefore, in the following discussion, magnetite is considered the only viable crystalline phase affecting nucleation behavior to a significant extent (e.g. Hurwitz and Navon, 1994; Cluzel et al., 2008).

The argument that oxides are completely lacking is usually based on the clear, homogeneous appearance of glass on the petrographic microscope or on SEM images. In experiments where the starting material undergoes thermal and or pressure treatments well above the liquidus (e.g. Mangan and Sisson, 2000; Iacono Marziano et al., 2007; Hamada et al., 2010), magnetite – if initially present – is unlikely to survive and

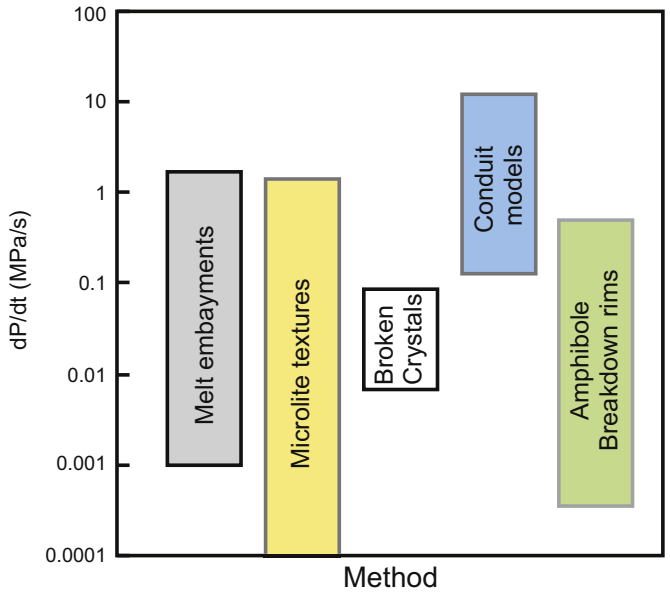


**Fig. 7.** Existing estimates of decompression rates of natural magmas involved in explosive eruptions calculated by various methods*. Only the ranges are shown for each method. *Values are from: embayments: Liu et al. (2007); Humphreys et al. (2008); Lloyd et al. (2014); Ferguson et al. (2016); Myers et al. (2016). Microlite textures: Couch et al. (2003); Castro and Gardner (2008); Andrews (2014); Szramek (2016). Broken crystals: Miwa and Geshi (2012). Conduit models: Papale and Dobran (1993); Kaminski and Jaupart (1997); Papale et al. (1998). Amphibole breakdown: Rutherford and Hill (1993); Rutherford and Devine (2003); Nicholis and Rutherford (2004); Rutherford (2008).

may indeed be absent at the beginning of decompression. In natural samples, however, Fe-Ti oxides are at least common as phenocryst or microphenocryst phases. In fact, they have been used for oxide thermo-oxybarometry for numerous eruptions involving rhyolite melt including Mt. Mazama 7.7 ka, Taupo 181 CE, Askja 1875 CE, Novarupta 1912 CE, Mt. St Helens 1980 CE, Pinatubo 1991 CE, Soufriere Hill 1997 CE, and Chaitén 2008 CE (e.g. Sigurdsson and Sparks, 1981; Bacon and Druitt, 1988; Rutherford and Hill, 1993; Sutton et al., 1995; Pallister et al., 1996; Hammer et al., 2002; Devine et al., 2003; Barker et al., 2014). Hence, magnetite is usually a stable phase prior to ascent of magmas that have been inferred to commonly foster homogeneous bubble nucleation.

The argument that the abundance or number of oxides is far lower than that of vesicles is also contentious because oxides are typically much smaller than bubbles and thus less likely to be intersected. To illustrate this problem, a volume of 240 × 240 × 240 μm containing three bubble populations with sizes of 10, 20, and 30 μm and an oxide population 2 μm in size was created numerically. A total of 3500 bubbles and the same number of oxides were distributed evenly in this volume so that $N_V^{oxides} = N_V^{bubbles} = 2.5 \times 10^5\ mm^{-3}$, and the volume was randomly sectioned (Fig. 8). In the example shown, a 2D image would display ~10–15 times fewer oxides than bubbles, and give areal number densities $N_A^{oxides} = 208\ mm^{-2}$ and $N_A^{bubbles} = 2900\ mm^{-2}$. This simple exercise highlights the well-known issue of intersection probability in the textural analysis literature (e.g. Saltikov, 1967; Cashman, 1990; Sahagian and Proussevitch, 1998). Therefore, having visibly fewer oxides in BSE images or even 30 μm thin sections does not preclude their presence in equal numbers in 3D.

Finally, studies have shown that magnetite populations can be present in sizes well below to the sub-micron range. Schlinger and Smith (1986), Schlinger et al. (1988) and Worm and Jackson (1999) used the superparamagnetic properties of <100 nm oxides to recover oxide size distributions in pyroclasts originating from different tuffs. They found that in glassy samples that had cooled more rapidly, most oxides were <20 nm in size. Mujin and Nakamura (2014) also report oxides down to ~20 nm in size within clasts from Vulcanian explosions in 2011 at Shinmoedake (Japan) with number densities far higher than any bubble number density measured in natural pumice. Thus, as previously suggested by Larsen (2008) it is possible that pyroclasts may contain a significant number of oxides that are simply too difficult to see by traditional observation. Whether such oxide nanolite populations form at depth or shortly before/after fragmentation is still unclear. Therefore, both documenting the presence and distribution of Fe-Ti oxides in pyroclasts and understanding their crystallization history relative to ascent and degassing are critical if we are to understand bubble nucleation processes in magma.

### 4.2. Potential effect of melt structure on nucleation

The exact influence of melt structure on the formation of critical clusters required for nucleation is physically poorly understood. Melt relaxation timescales calculated based on the Maxwell relationship $\tau_{relax} = \frac{\eta}{G_\infty}$ ($\eta$ is Newtonian viscosity of the relaxed melt, $G_\infty$ is the unrelaxed elastic shear modulus usually assumed to be about 10 GPa) are extremely short, in the order of nanoseconds, and are often taken to represent the time necessary for organization of the melt structure (cf. Dingwell, 1995). If this were the case, the superliquidus treatment of a crystal-free melt (e.g. the extent and duration of superheating) should bear no influence on subsequent phase transition kinetics (e.g. Vetere et al., 2013). On the contrary, experimental studies of crystallization have repeatedly demonstrated that extensive superheating treatments tend to delay nucleation and thereby influence growth behavior (e.g. Walker et al., 1978; Donaldson, 1979; Sato, 1995; Pupier et al., 2008; Leonhardi et al., 2015). A number of experimental studies in silicate and ceramic melts also reported relaxation timescales orders of magnitude longer than those predicted by the Maxwell relationship (Levelut et al., 2006; Malfait and Halter, 2008; Fu et al., 2013). Therefore, some of the melt structuring process may take place at different length and timescales than those considered by current relaxation models.

Following the lessons largely learned so far from crystallization experiments, the structural state of the melt prior to decompression may be just as important as Fe-Ti oxides in the context of bubble nucleation. Hurwitz and Navon (1994) noticed that even in experimental glasses visually devoid of crystals or oxides, nucleation occurred heterogeneously. Either oxides were there but too small to be seen, or, alternatively, the presence of a pre-decompression melt structure played an important role during nucleation. Gardner et al. (1999) also found that nucleation behavior depended on how long the melts were hydrated at the initial conditions under superliquidus conditions. Rhyolite melts that had dwelled for 3 days at the starting pressure appeared to nucleate heterogeneously, whereas those left for longer periods seemed to nucleate homogeneously (Fe-Ti oxides were not detected in those charges). Presumably, the longer superliquidus treatment served to eliminate the pre-existing melt structure and/or any sub-visible Fe-Ti oxides. In practice, this problem is well-known to experimentalists, who use superheating treatments to anneal any potential heterogeneities and favor homogeneous nucleation (e.g. Mangan and Sisson, 2000; Mourtada-Bonnefoi and Laporte, 2004; Iacono Marziano et al., 2007; Cichy et al., 2011). While such procedures are essential to adequately investigate the physics of homogeneous nucleation, natural melts unlikely experience such superliquidus treatments (i.e., superheating of >150–200 °C above the liquidus). Therefore, the direct transferability of homogeneous nucleation experiments to magma ascent during natural eruptions may be limited, and there is a pressing need to examine the specific role of melt structure on bubble nucleation.

### 4.3. Applications of nucleation models to natural magmas: the meaning and use of bubble number density

Bubble number densities measured in natural pyroclasts are often plotted against parameters such as melt $SiO_2$ or proxies for intensity

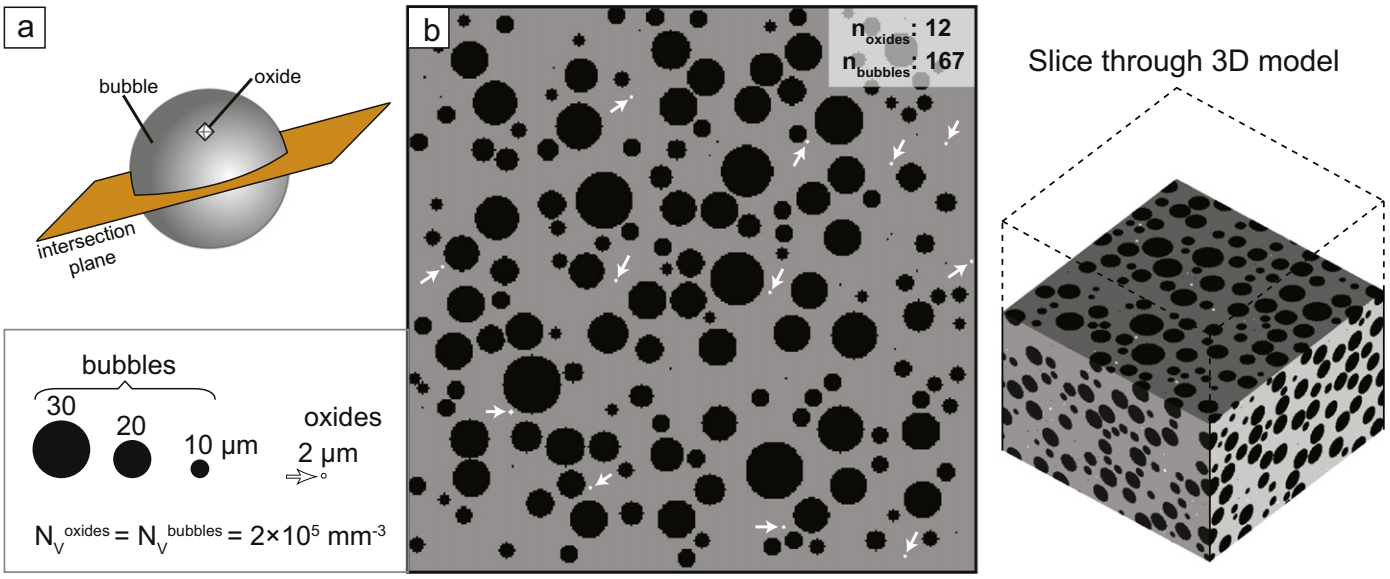


**Fig. 8.** (a) Illustration of intersection probability problems when considering small objects like Fe-Ti oxides in vesicular glass. The likelihood that a random section plane (orange) will intersect an oxide that may be located on a bubble wall is very low. (b) A 2D section through a 3D virtual pyroclast (here bubbles are spherical and are not allowed to touch/coalesce) constructed with 3500 bubbles of three sizes randomly placed within the melt along with 3500 small Fe-Ti oxides. This example highlights that far fewer oxides ($n_{oxides}$) will be observed on a typical thin section compared to vesicles ($n_{bubbles}$) due to the size-dependence of intersection probability.

such as eruption column height, or magma discharge rate $\dot{m}$ to test for possible correlations (e.g., Sable et al., 2006; Toramaru, 2006; Gurioli et al., 2008; Houghton et al., 2010; Rust and Cashman, 2011; Alfano et al., 2012; Pardo et al., 2014; Cashman and Mangan, 2014). The correlations are typically weak, which is not so surprising considering $N_V$ depends not on one but on all the parameters laid out in Eqs. (1) and (11). For instance eruption column height and magma discharge rates directly depend on magma decompression rates close to the surface, and melt composition partly controls parameters like water diffusivity. As discussed in previous sections, number densities should correlate well with decompression rates, though differently for different melt compositions. The calculations performed for the various eruptions examined here verify this relationship (Fig. 9a), and simple power-law expressions can be used to predict decompression rates from bubble number densities for different melt types:

$$\frac{dP}{dt} = \left(\frac{N_V}{A \times 10^4}\right)^{\frac{2}{3}} \tag{15}$$

where A equals 0.5(±0.35), 3(±1.8), and 15(±10) for basaltic/basaltic-andesitic, phonolitic/trachytic, and rhyolite melts respectively. This equation lumps a number of parameters into $A$, and for more precise estimates of $dP/dt$, the full Toramaru (2006) model (Eq. (11)) is preferred (cf. calculation spreadsheet available in the Supplementary material).

In its most basic form, mass discharge rate $\dot{m}$ is the product of volumetric flow rate $\dot{V}$ and magma density $\rho_{magma}$, which can be written as a function of decompression rate $dP/dt$, pressure gradient in the conduit $dP/dz$, and conduit radius $r$:

$$\dot{m} = \rho_{magma}\left(\frac{dP}{dz}\right)^{-1}\frac{dP}{dt}\cdot\pi r^2 \tag{16}$$

If an average, constant pressure gradient $dP/dz = 0.03$ MPa m$^{-1}$ is chosen along with a bulk (i.e. melt + vesicles ± crystals) magma density $\rho_{magma} = 1500$ kg m$^{-3}$, decompression rates calculated from $N_V$ can be used to obtain either magma discharge rate $\dot{m}$ or effective conduit radius $r$ (assuming the other can be estimated). For the eruptions studied here, magma discharge rates are available and correlate somewhat weakly with decompression rates calculated assuming heterogeneous nucleation dominated (Fig. 9b). This observation can be better understood if one considers that conduit radius varied substantially among these eruptions. For instance, the relationship between discharge rates and decompression rates for non-Plinian basaltic eruptions works well for effective conduit radii between 1 and 10 m (Fig. 9b), which, although an oversimplification of typical basaltic fissure-style conduit geometries, are dimensionally realistic (e.g. Wilson and Head, 1981). Basaltic, phonolitic, trachytic, and rhyolitic Plinian eruptions all require larger conduits (~10–150 m) to explain the relationship between $\dot{m}$ and $dP/dt$ observed. Two eruptions (Vesuvius 512 CE, Soufriere Hills 1997 CE) and eruption phases (phases B and C of Askja 1875 CE and units 4 and 4 of Taupo 181 CE) require conduit diameters that are unrealistically low (4–9 m). Similarly, the effective conduit diameter predicted for the 39 ka Campanian Ignimbrite (~40 m) is clearly an underestimate, even if the magma was erupted along numerous, extended but fairly narrow caldera fissures. In doing this exercise it should be noted that: (1) decompression rates calculated via $N_V$ are likely maximum values, but magma discharge rates are integrated averages, which may explain the small conduit diameters calculated for certain eruptions; (2) changing $dP/dz$ by a factor of 3 or the magma density $\rho_{magma}$ by ±500 kg m$^{-3}$ does not affect these observations significantly (Fig. 9b); and (3) assuming homogeneous instead of heterogeneous nucleation would lead to even smaller, more improbable values of conduit radius.

Despite the current uncertainties inherent to decompression rate calculations, these examples demonstrate the great potential of textural measurements such as bubble number density to retrieve physical parameters essential to characterize volcanic eruptions. Improving our ability to predict which nucleation mechanism dominates during magma ascent and apply correct values of surface tension for modeling purposes will ultimately provide volcanologists with texture-based tools to estimate ranges in magma discharge rate, conduit radius, and eruption column height. Such estimates are invaluable, particularly for pre-historical eruptions for which we possess little to no information. Physical parameters are also difficult to obtain for submarine explosive eruptions through classical field methods, and the capacity to correctly interpret and use bubble number densities could help resolve debates about eruption dynamics (e.g. Shea et al., 2013).

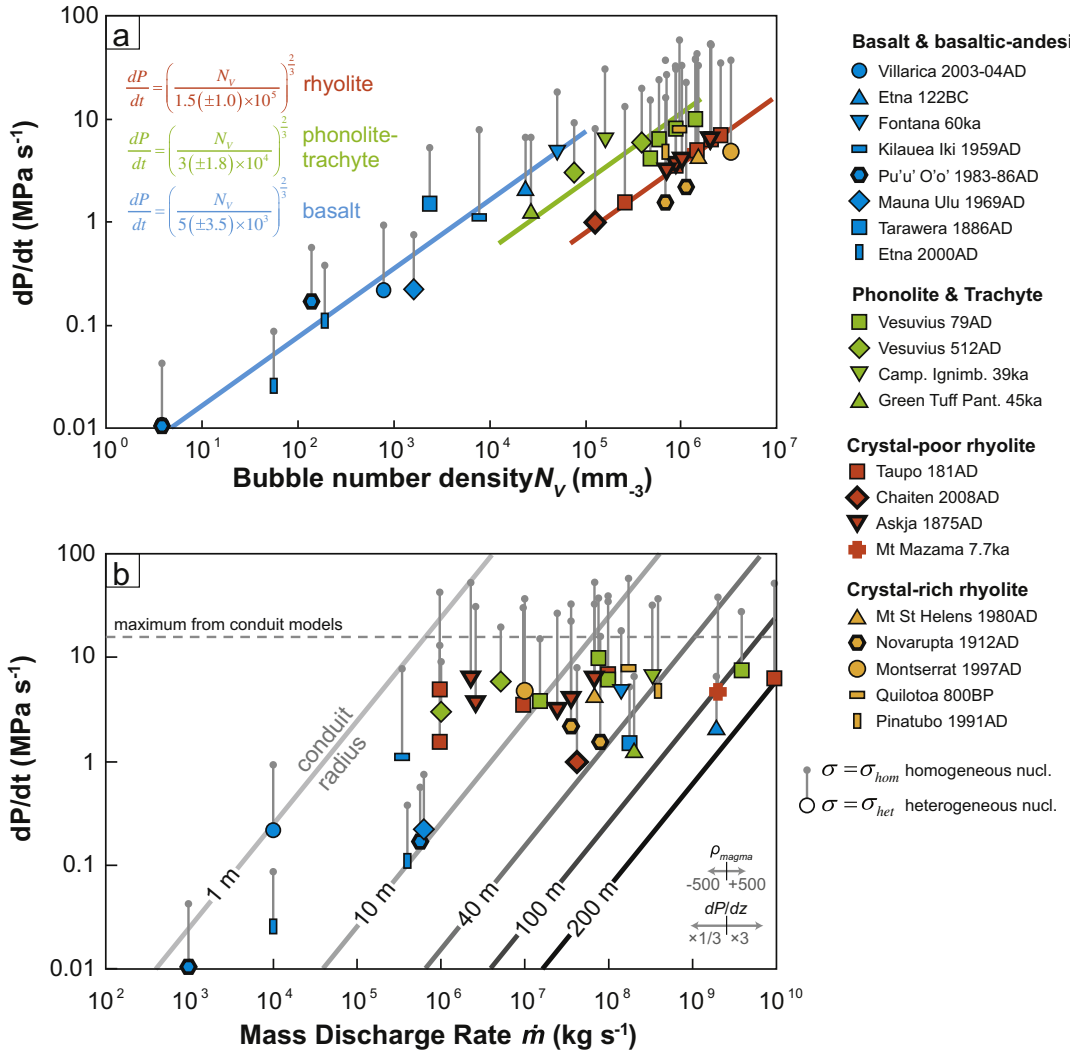


**Fig. 9.** The use of bubble number density to calculate decompression rates from natural pyroclasts, and their correlation with key eruption parameters such as discharge rate. (a) Bubble number densities correlate well with decompression rates as expected from Eq. (11), and simple power-law empirical fits provide reasonable first-order estimates for different melt compositions. (b) Mass discharge rates obtained from deposit volumes and eruption timing show a crude correlation with *dP*/*dt*, partly because mass discharge rates depend on both *dP*/*dt* and effective conduit radius. Gray and black lines show effective radii calculate for a given set of MDR and *dP*/*dt* values (Eq. (16)). Gray horizontal arrows display the change in ṁ resulting from large variations in magma density $\rho_{magma}$ or pressure gradient *dP*/*dz*. Thin gray lines with gray dots report *dP*/*dt* values obtained using surface tension values associated with homogeneous nucleation, while all color symbols use the heterogeneous nucleation assumption. Assuming homogeneous nucleation in calculations of *dP*/*dt* leads to values that are far above estimates from other methods, including from conduit models (horizontal dashed gray line, cf. Fig. 7).

### *4.4. Consequences of nucleation mechanism on degassing style*

Homogeneous nucleation has been proposed to be partially responsible for magma explosivity towards the surface (Mourtada-Bonnefoi and Laporte, 1999; Mangan and Sisson, 2000). In this scenario, difficulties in nucleating bubbles without attaining large (>100 MPa) values of supersaturation would cause magmas to follow degassing paths far from equilibrium. The ensuing delay in water exsolution in turn results in sudden vesiculation as soon as $\Delta P_N$ is reached, promoting high intensity explosive eruptions (Mangan and Sisson, 2000; Mourtada-Bonnefoi and Laporte, 2004). Because supersaturation pressures for nucleation were found to be higher for rhyolite melts than for other compositions such as dacite, homogeneous nucleation and non-equilibrium degassing would therefore explain why rhyolites fuel the most explosive eruptions (Mangan et al., 2004).

Alkalic magmas such as phonolites and trachytes provide counterexamples to this axiom. These magmas are not particularly viscous compared to rhyolites (e.g. Shea et al., 2017), have been shown to foster heterogeneous nucleation and degas closer to equilibrium than their calc-alkalic counterparts (e.g. Shea et al., 2010a), but still produce some of the highest intensity eruptions worldwide (e.g. Campanian Ignimbrite 39 ka, Vesuvius 79 CE, Tambora 1815 CE in Indonesia, Laacher See 12.9 ka in Germany, Abrigo 190 ka in Tenerife). Hence, homogeneous nucleation and highly non-equilibrium degassing is not a sine qua non for high magma explosivity.

## 5. Perspectives

### *5.1. Should the classical nucleation theory still be utilized?*

Models based on macroscopic measurements (Eq. (12) and Bagdassarov et al., 2000) were shown here to greatly overestimate experimental surface tension values recovered from back-solving the classical nucleation equation (Eq. (1)) (cf. Fig. 4 and Hamada et al., 2010; Gardner et al., 2013). Colucci et al. (2016) recently tested more sophisticated expressions for surface tension based on gradient phase theory that reproduced macroscopic measurements adequately, and reached similar conclusions. Problems with matching estimates of interfacial

energy calculated from nucleation theory with macroscopic data are not unique to bubbles, as similar issues also impair our understanding of crystal nucleation in magmas (e.g. Hammer, 2008). Hammer (2004) suggested that perhaps the classical nucleation theory was inadequate to accurately describe crystal nucleation in silicate melts, and that interfacial energy values calculated from solving the CNT may simply amass the uncertainties and interdependencies of various parameters (i.e. a 'fudge' factor). Our difficulties in predicting values of surface tension for homogeneous nucleation and understanding composition-, temperature-, and pressure-dependence could therefore stem from problems with classical nucleation theory itself. Gonnermann and Gardner (2013) explored this hypothesis and found that nonclassical theory could better explain the discrepancy between macroscopic measurements and surface tension values calculated from experimental nucleation rates. While their approach may be key to understanding the tenets of homogeneous nucleation in magmas, the formalism of nonclassical nucleation currently still relies on solving for another parameter ($\Delta P^*$, the "reference pressure" or the difference between the pressure inside the nucleus and pressure at the spinodal, Gonnermann and Gardner, 2013) that we cannot easily determine. Until further progress has been made to improve our predictive ability for values of surface tension for homogeneous nucleation that are well recovered by experiments, empirical fits such as Eq. (13) can be used with the classical nucleation theory as first order estimates for $\sigma_{hom}$. In practice, the CNT is better utilized to estimate supersaturation pressures required for nucleation (e.g. Fig. 5) rather than to compute rates of nucleation (e.g. Mourtada-Bonnefoi and Laporte, 2004; Cluzel et al., 2008; Hamada et al., 2010; Gardner et al., 2013).

### 5.2. Experimental priorities

Bubble nucleation equations are increasingly implemented within numerical models that simulate magma ascent and degassing (e.g., Gonnermann and Manga, 2013; Campagnola et al., 2016), and the great potential of using easily-obtained textural parameters to extract physical eruption parameters has been highlighted throughout this contribution. While existing gaps in variables controlling nucleation like water diffusivity/solubility, melt density, saturation pressure, temperature have been filled significantly in the last two decades, the current state of uncertainty surrounding surface tension and its derivatives (supersaturation pressures or decompression rates) remains problematic (e.g. Figs. 4 and 6). Part of the problem lies with understanding and isolating the main variables within experimental studies. Therefore, 'ideal' suites of experiments should attempt to isolate a number of key factors, which I list here by their inferred order of importance:

- *The effect of magnetite*: Hurwitz and Navon (1994) and Gardner and Denis (2004) are still to date the only comprehensive examinations of heterogeneous nucleation on magnetite. Cluzel et al. (2008) found the influence of hematite to be far less significant. Future experiments should focus on resolving the pre- and post-decompression size and number distributions of magnetite (cf. Section 5.3 below) and on attempting to elucidate whether magnetite populations are already present prior to magma ascent, or whether the bulk of them form during degassing - in which case their influence on nucleation may be subdued. A key step and difficulty in performing optimum experiments involves controlling $fO_2$ precisely to allow variations in oxide population characteristics to be imposed.
- *The effect of pre-decompression superliquidus treatments*: How far near or above the liquidus should the charge be hydrated to (1) best replicate natural magmas, or (2) best simulate homogeneous nucleation. Does the use of synthetic vs. natural starting material matter? These matters are likely critical in controlling nucleation but have so far not been investigated.
- *The effect of decompression rate and style*: Several studies have highlighted differences in textures obtained via SSD, MSD and CD, and the unsuitable nature of SSD to simulate nucleation in nature (cf. Marxer et al., 2015; Fiege and Cichy, 2015). In theory, however, decompressing a melt instantly and quenching after various dwell times is the only way to determine its response to a given pressure perturbation $\Delta P$ accurately (e.g. Hammer, 2008; Shea and Hammer, 2013 in the case of crystal nucleation). Less instantaneous decompression experienced during MSD or CD runs can lead to diffusion of $H_2O$ towards the capsule-melt interface and either heterogenous nucleation or expansion of free vapor in the capsule (e.g. Mangan and Sisson, 2000; Iacono Marziano et al., 2007; Marxer et al., 2015). Therefore, SSD experiments should still be prioritized if the objective is to quantify supersaturation pressures for nucleation and thereby effective values of surface tension. SSD, on the other hand, are not well-suited to investigate the effect of decompression rate on bubble number densities (Fig. 6), and CD should be used instead.
- *The effect of melt composition*: Gardner et al. (2013) examined the potential effect of melt composition on surface tension and found no convincing relationship, contrary to the compilation presented herein (Fig. 4) and other studies (Mangan et al., 2004; Gardner and Ketcham, 2011). In their study, melt temperature was set at 1150–1200 °C to isolate the effects of temperature from those of composition. In doing so, melts with lower liquidus temperatures (rhyolite, dacite, trachyte) experienced superliquidus treatments that could have impacted their pre-decompression structure to a greater extent compared to the less evolved melts with higher liquidus (basalt, phonotephrite). Compositional dependence, or lack thereof, therefore requires experimental confirmation, possibly by subjecting melts to pre-decompression temperatures at similar values of superheating $\Delta T_L = T - T_{liquidus}$ rather than the same temperature, at the risk of not isolating the effects of temperature itself. As argued below, absolute temperature effects on surface tension are likely less easily tractable than other factors listed here.
- *The effect of other volatile species*: Herein, $H_2O$ was inferred to control final bubble number densities measured in pyroclasts. This assumption is valid for melts that are mostly water-saturated, particularly rhyolites (e.g. Chaiten, Soufriere Hills, Novarupta, Taupo, Mazama), but debatable for other less evolved magmas that often contain more $CO_2$ or $SO_2$ (Etna 122 BCE, Kilauea eruptions, Stromboli). For instance, increases in bubble number densities were recently reported in decompression experiments involving $SO_2$-rich andesite melts (Fiege et al., 2014). The effect of adding low $CO_2$ contents (few tens of ppm) to a mostly water-saturated melt seems to be restricted to retarding bubble growth once nucleation has occurred (e.g. Gonnermann and Houghton, 2012). At higher concentrations (>800 ppm), $CO_2$ appears to cause further delays for homogeneous nucleation, requiring larger $\Delta P_N$ (Mourtada-Bonnefoi and Laporte, 2002). For Strombolian or Hawaiian basaltic eruptions involving initially $CO_2$-rich magmas, shallow $H_2O$ exsolution provides the main drive for explosive activity ($H_2O$ constitutes 80 mol% by volume of the total exsolved gas) (Gerlach, 1986; Mangan et al., 1993), therefore the influence of $CO_2$ on pyroclast bubble number densities is likely minor. A critical unknown in the few existing studies involving $CO_2$ (Mourtada-Bonnefoi and Laporte, 1999, 2002; Pichavant et al., 2013) is whether changes in nucleation behavior are driven by the presence of $CO_2$ itself or by the undersaturated nature of the melt with respect to $H_2O$. To better understand the role of other volatiles on bubble nucleation, experiments should also focus on isolating the effect of $H_2O$ undersaturation (i.e. a melt that only contains $H_2O$, but below saturation level) from that of introducing other species (i.e. a melt that contains the same amount of $H_2O$ mixed with another volatile species), as was done by Fiege et al. (2014) for $H_2O$ and $SO_2$.
- *The effect of temperature*: The true effect of temperature on surface tension may be the most difficult to isolate from other variables, since temperature probably controls pre-decompression melt structure/homogeneity, in addition to water solubility, diffusivity, and melt viscosity. Gardner and Ketcham (2011) investigated

temperature dependence of surface tension for rhyolite between 775 °C and 1080 °C, and proposed a complex behavior where temperature effects equaled those measured by Bagdassarov et al. (2000) at low viscosities (~$7 \times 10^{-5}$ N $m^{-1}$/°C for $\eta < 10^4$ Pa s) but failed to obey any relationship at higher viscosities. Future experiments focused on less viscous basaltic-andesitic or basaltic melts could help circumvent this viscosity problem whilst allowing for a wide range of temperatures to be investigated (e.g. 1000–1300 °C).

### 5.3. Exploring the submicron scale

The lack of direct observations of the initial stages of nucleation significantly hampers our understanding of how clusters of atoms become a nucleus. Whereas Transmission Electron Microscopy (TEM) has been used extensively in engineered materials to image crystal nuclei at the atom scale (Riello et al., 2001; Dargaud et al., 2011; Höche, 2010; Patzig et al., 2012), similar investigations are still lacking in the fields of magma crystallization/vesiculation. Earlier studies of Schlinger et al. (1991), Besson and Poirier (1994), Sharp et al. (1996) illustrated the potential of detailed TEM analysis to examine micro-to-nanoscale crystals in volcanic rocks, including Fe-Ti oxides; since then, however, few efforts have attempted to identify crystal- or bubble-forming clusters. Frontier TEM investigations imaging combined with structural information obtained by spectroscopy techniques (XANES, microRaman, TEM-EELS) have the potential to resolve critical questions pertaining to the critical cluster size and shape, as well as the structural changes that the melt needs to undergo during a given phase transition (e.g. Hu et al., 2005; Bhattacharyya et al., 2009). Due to its large density contrast with most surrounding phases, magnetite can also be easily detected and imaged by 3D by X-ray microtomography down to sizes ~200 nm (e.g. Gualda et al., 2010; Einsle et al., 2016). Moreover, owing to its unique magnetic properties, magnetite can be fully characterized down to sizes of a few nm within pyroclasts using a variety of magnetism experiments (Schlinger et al., 1988; Worm and Jackson, 1999). Combining these direct measurements of oxide and silicate glass properties will be essential to appreciate (1) the nature of the nucleus-melt interface (abrupt, which is the assumption adopted in the CNT, or diffuse, the basis of non-classical theory), (2) the influence of the structural state of the melt on nucleation, and (3) how pervasive and small Fe-Ti oxides really are in natural and experimental melts.

## 6. Conclusions

Bubble nucleation is a fundamental aspect of magma ascent and volcanism, yet its homogeneous or heterogeneous character in natural magmas remains to be established. Thorough tests of the nucleation theory and other rate-meters based on nucleation models expose important inconsistencies with the assumption of homogeneous nucleation. Supersaturation pressures for homogeneous nucleation are in some cases close to or even larger than the inferred storage pressure, and decompression rates attain values that are unrealistically high. The idea that magma degassing is altogether delayed by the high supersaturation requirements until fairly shallow levels also contradicts the notion that magma ascent towards the surface is driven in the first place by volatile exsolution, expansion, and in many cases overpressurization (e.g. Gonnermann and Manga, 2013).

Previous studies have highlighted the dominance of homogeneous nucleation in most magmas lacking microlites. In this contribution, some of the arguments against heterogeneous nucleation were reviewed and found to be generally inconclusive. It is proposed instead that nucleation may well be heterogeneous throughout the realm of silicate melts involved in most eruptions, and that only through careful examination of magnetite content and melt structure at the nanometer scale will it be possible to provide a more conclusive answer. Finally, suggestions were provided for experimental priorities that may help elucidate the intertwined roles of magnetite, melt structure, melt composition, decompression rate, mixed volatile species, and magma temperature on nucleation. Solving the nucleation mechanism conundrum is essential to our understanding of magma degassing and holds the promise of direct applications to quantifying essential physical parameters of natural eruptions (decompression rate, discharge rate, conduit radius, eruption column height) by simply measuring bubble number densities in pyroclasts.

## Acknowledgements

This work was funded by NSF Grant EAR-1321890. Many of the ideas developed for this paper, particularly those regarding heterogeneous nucleation were 'seeded' during numerous discussions with Jessica Larsen. Input from Julia Hammer and Jim Gardner on bubble and crystal nucleation over the recent years has been of great value. I thank two anonymous reviewers for their constructive comments and editor J. Gardner for efficient handling of the manuscript.

## Appendix A. Supplementary data

Supplementary data to this article can be found online at http://dx.doi.org/10.1016/j.jvolgeores.2017.06.025.

## References

Adams, N.K., Houghton, B.F., Fagents, S.A., Hildreth, W., 2006. The transition from explosive to effusive eruptive regime: the example of the 1912 Novarupta eruption, Alaska. Geol. Soc. Am. Bull. 118:620–634. http://dx.doi.org/10.1130/B25768.1.

Alfano, F., Bonadonna, C., Gurioli, L., 2012. Insights into eruption dynamics from textural analysis: the case of the May, 2008, Chaitén eruption. Bull. Volcanol. 74, 2095–2108.

Andrews, B.J., 2014. Magmatic storage conditions, decompression rate, and incipient caldera collapse of the 1902 eruption of Santa Maria Volcano, Guatemala. J. Volcanol. Geotherm. Res. 282, 103–114.

Andujar, J., Scaillet, B., 2012. Relationships between pre-eruptive conditions and eruptive styles of phonolite–trachyte magmas. Lithos 152, 122–131.

Bacon, C.R., Druitt, T.H., 1988. Compositional evolution of the zoned calcalkaline magma chamber of Mount Mazama, Crater Lake, Oregon. Contrib. Mineral. Petrol. 98: 224–256. http://dx.doi.org/10.1007/BF00402114.

Bagdassarov, N., Dorfman, A., Dingwell, D., 2000. Effect of alkalis, phosphorus, and water on the surface tension of haplogranite melt. Am. Mineral. 85, 33–40.

Bakker, R.J., 2003. Package FLUIDS: 1, computer programs for analysis of fluid inclusion data and for modeling bulk fluid properties. Chem. Geol. 194, 3–23.

Barker, S.J., Wilson, C.J.N., Smith, E.G.C., Charlier, B.L.A., Wooden, J.L., Hiess, J., Ireland, T.R., 2014. Post-supereruption magmatic reconstruction of Taupo volcano (New Zealand), as reflected in zircon ages and trace elements. J. Petrol. 55, 1511–1533.

Besson, P., Poirier, J.-P., 1994. The 3100 BP eruption of the Soufriere of Guadeloupe, a transmission electron microscope study of the cryptodome andesite. Bull. Volcanol. 56, 184–192.

Bhattacharyya, S., Höche, T., Hemono, N., Pascual, M.J., van Aken, P.A., 2009. Nano-crystallization in $LaF_3$-$Na_2O$-$Al_2O_3$-$SiO_2$ glass. J. Cryst. Growth 311, 4350–4355.

Blundy, J., Cashman, K.V., Berlo, K., 2008. Evolving magma storage conditions beneath Mount St. Helens inferred from chemical variations in melt inclusions from the 1980–1986 and current (2004–2006) eruptions. In: Sherrod, D.R., Scott, W.E., Stauffer, P.H. (Eds.), A Volcano Rekindled: The Renewed Eruption of Mount St. Helens, 2004–2006: U.S. Geological Survey Professional Paper. 1750 (36 pp.).

Bouvet de Maisonneuve, C., Bachmann, O., Burgisser, A., 2009. Characterization of juvenile pyroclasts from the Kos Plateau Tuff (Aegean arc): insights into the eruptive dynamics of a large rhyolitic eruption. Bull. Volcanol. 71, 643–658.

Campagnola, S., Romano, C., Mastin, L.G., Vona, A., 2016. Confort 15 model of conduit dynamics: applications to Pantelleria Green Tuff and Etna 122 BC eruptions. Contrib. Mineral. Petrol. 171:60. http://dx.doi.org/10.1007/s00410-016-1265-5.

Carey, R.J., Houghton, B.F., Thordarson, T., 2009. Abrupt shifts between wet and dry phases of the 1875 eruption of Askja volcano: microscopic evidence for macroscopic dynamics. J. Volcanol. Geotherm. Res. 184:256–270. http://dx.doi.org/10.1016/j.jvolgeores.2009.04.003.

Carroll, M.R., Blank, J.G., 1997. The solubility of $H_2O$ in phonolitic melts. Am. Mineral. 82, 549–556.

Cashman, K., 1990. Textural constraints on the kinetics of crystallization of igneous rocks. Rev. Mineral. 24, 259–314.

Cashman, K.V., Mangan, M.T., 2014. A century of studying effusive eruptions in Hawai'i. Characteristics of Hawaiian volcanoes. U.S.G.S. Prof. Paper 1801-9:357–394. http://dx.doi.org/10.3133/pp18019.

Castro, J.M., Gardner, J.E., 2008. Did magma ascent rate control the explosive-effusive transition at the Inyo volcanic chain, California? Geology 36, 279–282.

Cichy, S.B., Botcharnikov, R.E., Holtz, F., Behrens, H., 2011. Vesiculation and microlite crystallization induced by decompression: a case study of the 1991-95 Mt Unzen eruption (Japan). J. Petrol. 52, 1469–1492.

Cioni, R., 2000. Volatile content and degassing processes in the AD 79 magma chamber at Vesuvius (Italy). Contrib. Mineral. Petrol. 140, 40–54.

Cluzel, N., Laporte, D., Provost, A., Kannewischer, I., 2008. Kinetics of heterogeneous bubble nucleation in rhyolitic melts: implications for the number density of bubbles in volcanic conduits and for pumice textures. Contrib. Mineral. Petrol. 156, 745–763.

Colombier, M., Gurioli, L., Druitt, T.H., Shea, T., Boivin, P., Miallier, D., Cluzel, N., 2017. Textural evolution of magma during the 9.4-ka trachytic explosive eruption at Kilian Volcano, Chaine des Puys, France. Bull. Volcanol. 79, 17.

Colucci, S., Battaglia, M., Trigila, R., 2016. A thermodynamical model for the surface tension of silicate melts in contact with $H_2O$ gas. Geochim. Cosmochim. Acta 175: 113–127. http://dx.doi.org/10.1016/j.gca.2015.10.037.

Costantini, L., Houghton, B.F., Bonadonna, C., 2010. Constraints on eruption dynamics of basaltic explosive activity derived from chemical and microtextural study: the example of the Fontana Lapilli Plinian eruption, Nicaragua. J. Volcanol. Geoth. Res. 189, 207–224.

Couch, S., Sparks, R.S.J., Carroll, M.R., 2003. The kinetics of degassing-induced crystallization at Soufriere Hills Volcano, Montserrat. J. Petrol. 44, 1477–1502.

Dargaud, O., Cormier, L., Menguy, N., Patriarche, G., Calas, G., 2011. Mesoscopic scale description of nucleation processes in glasses. Appl. Phys. Lett. 99, 021904.

Del Carlo, P., Pompilio, M., 2004. The relationship between volatile content and the eruptive style of basaltic magma: the Etna case. Ann. Geophys. 47, 1423–1432.

Devine, J.D., Rutherford, M.J., Norton, G.E., Young, S.R., 2003. Magma storage region processes inferred from geochemistry of Fe–Ti oxides in andesitic magma, Soufrière Hills Volcano, Montserrat, W.I. J. Petrol. 44, 1375–1400.

Di Matteo, V., Carroll, M.R., Behrens, H., Vetere, F., Brooker, R.A., 2004. Water solubility in trachyte melts. Chem. Geol. 213, 187–196.

Dingwell, D.B, 1995. Relaxation in silicate melts: Some applications. In: Stebbins, J., McMillan, P.F., Dingwell, D.B. (Eds.), Structure, dynamics and properties of silicate melts. Rev. Mineral 32, pp. 21–26.

Donaldson, C.H., 1979. An experimental investigation of the delay in nucleation of olivine in mafic magmas. Contrib. Mineral. Petrol. 69, 21–32.

Druitt, T.H., Mercier, M., Florentin, L., Deloule, E., Cluzel, N., Flaherty, T., Medard, E., Cadoux, A., 2016. Magma storage and extraction associated with Plinian and Interplinian activity at Santorini caldera (Greece). J. Petrol. 57, 461–494.

Einsle, J.F., Harrison, R.J., Kasama, T., Conbhuí, P.Ó., Fabian, K., Williams, W., Wood-land, L., Fu, R.R., Weiss, B.P., Midgley, P.A., 2016. Multi-scale three-dimensional characterisation of iron particles in dusty olivine: implications for paleomag-netism of chondritic meteorites. Am. Mineral. 101, 2070–2084.

Fanara, S., Behrens, H., Zhang, Y., 2012. Water diffusion in potassium-rich phonolitic and trachytic melts. Chem. Geol. 346, 149–161.

Ferguson, D.J., Gonnermann, H.M., Ruprecht, P., Plank, T., Hauri, E.H., Houghton, B.F., Swanson, D.A., 2016. Magma decompression rates during explosive eruptions of Kilauea volcano, Hawaii, recorded by melt embayments. Bull. Volcanol. 78:71. http://dx.doi.org/10.1007/s00445-016-1064-x.

Fiege, A., Cichy, S.B., 2015. Experimental constraints on bubble formation and growth during magma ascent: a review. Am. Mineral. 100, 2426–2442.

Fiege, A., Holtz, F., Cichy, S.B., 2014. Bubble formation during decompression of andesitic melts. Am. Mineral. 99:1052–1062. http://dx.doi.org/10.2138/am.2014.4719.

Fu, X., Chen, G., Zu, Y., Luo, J., Zhou, W., 2013. Microstructure refinement of melt-grown Al2O3/YAG/ZrO2 eutectic composite by a new method: melt superheating treatment. Scr. Mater. 68, 731–734.

Gardner, J.E., 2012. Surface tension and bubble nucleation in phonolite magmas. Geochim. Cosmochim. Acta 76, 93–102.

Gardner, J.E., Denis, M.-H., 2004. Heterogeneous bubble nucleation on Fe–Ti oxide crystals in high-silica rhyolitic melts. Geochim. Cosmochim. Acta 68, 3587–3597.

Gardner, J.E., Ketcham, R.A., 2011. Bubble nucleation in rhyolite and dacite melts: temperature dependence of surface tension. Contrib. Mineral. Petrol. 162:929–943. http://dx.doi.org/10.1007/s00410-011-0632-5.

Gardner, J.E., Hilton, M., Carroll, M.R., 1999. Experimental constraints on degassing of magma: isothermal bubble growth during continuous decompression from high pressure. Earth Planet. Sci. Lett. 168, 201–218.

Gardner, J.E., Ketcham, R.A., Moore, G., 2013. Surface tension of hydrous silicate melts: constraints on the impact of melt composition. J. Volcanol. Geotherm. Res. 267, 68–74.

Gerlach, T., 1986. Exsolution of $H_2O$, $CO_2$, and S during eruptive episodes of Kilauea volcano, Hawaii. J. Geophys. Res. 91, 12177–12185.

Geschwind, C.H., Rutherford, M.J., 1995. Crystallization of microlites during magma ascent; the fluid mechanics of 1980–1986 eruptions at Mount St. Helens. Bull. Volcanol. 57, 356–370.

Giachetti, T., Druitt, T.H., Burgisser, A., Arbaret, L., Galven, C., 2010. Bubble nucleation, growth and coalescence during the 1997 Vulcanian explosions of Soufrière Hills volcano, Montserrat. J. Volcanol. Geotherm. Res. 193, 215–231.

Giachetti, T., Burgisser, A., Arbaret, L., Druitt, T.H., Kelfoun, K., 2011. Quantitative textural analysis of Vulcanian pyroclasts (Montserrat) using multi-scale X-ray computed microtomography: comparison with results from 2D image analysis. Bull. Volcanol. 73:1295–1309. http://dx.doi.org/10.1007/s00445-011-0472-1.

Gondé, C., Martel, C., Pichavant, M., Bureau, H., 2011. In situ bubble vesiculation in silicic magmas. Am. Mineral. 96, 111–124.

Gonnermann, H.M., Gardner, J.E., 2013. Homogeneous bubble nucleation in rhyolitic melt: experiments and nonclassical theory. Geochem. Geophys. Geosyst. 14:1–16. http://dx.doi.org/10.1002/ggge.20281.

Gonnermann, H.M., Houghton, B.F., 2012. Magma degassing during the Plinian eruption of Novarupta, Alaska, 1912. Geochem. Geophys. Geosyst. 13:1–20. http://dx.doi.org/10.1029/2012GC004273.

Gonnermann, H.M., Manga, M., 2013. Dynamics of magma ascent in the volcanic conduit. In: Fagents, S.A., Gregg, T.K.P., Lopes, R.M.C. (Eds.), Modeling Volcanic Processes, the Physics and Mathematics of Volcanism. Cambridge University Press, Cambridge, pp. 55–84.

Gualda, G.A.R., Pamukcu, A.S., Claiborne, L.L., Rivers, M.L., 2010. Quantitative 3D petrography using x-ray tomography. 3: documenting accessory phases with differential absorption tomography. Geosphere 6, 782–792.

Gurioli, L., Harris, A.J.L., Houghton, B.F., Polacci, M., Ripepe, M., 2008. Textural and geophysical characterization of explosive basaltic activity at Villarrica volcano. J. Geophys. Res. 113, B08206. http://dx.doi.org/10.1029/2007JB005328.

Hamada, M., Laporte, D., Cluzel, N., 2010. Simulating bubble number density of rhyolitic pumices from Plinian eruptions: constraints from fast decompression experiments. Bull. Volcanol. 3:735–746. http://dx.doi.org/10.1007/s00445-010-0353-z.

Hammer, J.E., 2004. Crystal nucleation in hydrous rhyolite: experimental data applied to classical theory. Am. Mineral. 89, 1673–1679.

Hammer, J.E., 2008. Experimental studies of the kinetics and energetics of magma crystallization. Rev. Mineral. 69:9–59. http://dx.doi.org/10.2138/rmg.2008.69.2.

Hammer, J.E., Rutherford, M.E., Hildreth, W., 2002. Magma storage prior to the 1912 eruption at Novarupta, Alaska. Contrib. Mineral. Petrol. 144, 144–162.

Hirth, G., Pound, G.M., St Pierre, G.R., 1970. Bubble nucleation. Metall. Trans. A. 1, 939–945.

Höche, T., 2010. Crystallization in glass: elucidating a realm of diversity by transmission electron microscopy. J. Mater. Sci. 45, 3683–3696.

Holloway, J.R., Blank, J.G., 1994. Application of experimental results to C-O-H species in natural melts. Rev. Mineral. 30, 187–230.

Houghton, B.F., Carey, R.J., Cashman, K.V., Wilson, C.J.N., Hobden, B.J., Hammer, J.E., 2010. Diverse patterns of ascent, degassing, and eruption of rhyolite magma during the 1.8 ka Taupo eruption, New Zealand: evidence from clast vesicularity. J. Volcanol. Geotherm. Res. 195, 31–47.

Hu, Z., Wang, Y., Bao, F., Luo, W., 2005. Crystallization behavior and microstructure investigations on LaF3 containing oxyfluoride glass ceramics. J. Non-Cryst. Solids 351, 722–728.

Humphreys, M., Menand, T., Blundy, J.D., Klimm, K., 2008. Magma ascent rates in explosive eruptions: constraints from $H_2O$ diffusion in melt inclusions. Earth Planet. Sci. Lett. 270, 25–40.

Hurwitz, S., Navon, O., 1994. Bubble nucleation in rhyolitic melts: experiments at high pressure, temperature, and water content. Earth Planet. Sci. Lett. 122, 267–280.

Iacono Marziano, G., Schmidt, B.C., Dolfi, D., 2007. Equilibrium and disequilibrium degassing of a phonolitic melt (Vesuvius AD 79 "white pumice") simulated by decompression experiments. J. Volcanol. Geotherm. Res. 161, 151–164.

Kaminski, E., Jaupart, C., 1997. Expansion and quenching of vesicular magma fragments in Plinian eruptions. J. Geophys. Res. 102, 12187–12203.

Khitarov, N.I., Lebedev, Y.B., Dorfman, A.M., Bagdasarov, N.S., 1979. Effects of temperature, pressure and volatiles on the surface tension of molten basalt. Geochem. Int. 16, 78–86.

Klug, C., Cashman, K.V., Bacon, C., 2002. Structure and physical characteristics of pumice from the climactic eruption of Mount Mazama (Crater Lake), Oregon. Bull. Volcanol. 64, 486–501.

Larsen, J.F., 2008. Heterogeneous bubble nucleation and disequilibrium $H_2O$ exsolution in Vesuvius K-phonolite melts. J. Volcanol. Geotherm. Res. 275, 278–288.

Larsen, J.F., Gardner, J.E., 2004. Experimental study of water degassing from phonolite melts: implications for volatile oversaturation during magmatic ascent. J. Volcanol. Geotherm. Res. 134, 109–124.

Le Gall, N., Pichavant, M., 2016a. Homogeneous bubble nucleation in $H_2O$- and $H_2O$-$CO_2$-bearing basaltic melts: results of high temperature decompression experiments. J. Volcanol. Geotherm. Res. 327, 604–621.

Le Gall, N., Pichavant, M., 2016b. Experimental simulation of bubble nucleation and magma ascent in basaltic systems: implications for Stromboli volcano. Am. Mineral. 101, 1967–1985.

Leonhardi, T.C., Hammer, J.E., First, E., 2015. Effect of Superheating on Olivine Nucleation and Growth in a Silica-Undersaturated Melt: An Experimental Study. AGU Abstract V41B-3071, Fall Meeting 2015, San Francisco, USA.

Levelut, C., Le Parc, R., Faivre, A., Champagnon, B., 2006. Influence of thermal history on the structure and properties of silicate glasses. J. Non-Cryst. Solids 352, 4495–4499.

Liu, Y., Zhang, Y., Behrens, H., 2005. Solubility of $H_2O$ in rhyolitic melts at low pressures and a new empirical model for mixed $H_2O$–$CO_2$ solubility in rhyolitic melts. J. Volcanol. Geotherm. Res. 143:219–235. http://dx.doi.org/10.1016/j.jvolgeores.2004.09.019.

Liu, Y., Anderson, A.T., Wilson, C.J.N., 2007. Melt pockets in phenocrysts and decompression rates of silicic magmas before fragmentation. J. Geophys. Res. 112, B06204. http://dx.doi.org/10.1029/2006JB004500.

Lloyd, A.S., Ruprecht, P., Hauri, E.H., Rose, W., Gonnermann, H.M., Plank, T., 2014. NanoSIMS results from olivine-hosted melt embayments: magma ascent rate during explosive basaltic eruptions. J. Volcanol. Geotherm. Res. 283, 1–18.

Malfait, W.J., Halter, W.E., 2008. Structural relaxation in silicate glasses and melts: high temperature Raman spectroscopy. Phys. Rev. 77, 014201.

Mangan, M.T., Sisson, T.W., 2000. Delayed, disequilibrium degassing in rhyolite magma: decompression experiments and implications for explosive volcanism. Earth Planet. Sci. Lett. 183, 441–455.

Mangan, M.T., Sisson, T.W., 2005. Evolution of melt-vapor surface tension in silicic volcanic systems: experiments with hydrous melts. J. Geophys. Res. 110, B01202.

Mangan, M.T., Cashman, K.V., Newman, S., 1993. Vesiculation of basaltic magma during eruption. Geology 21, 157–160.

Mangan, M.T., Sisson, T.W., Hankins, W.B., 2004. Decompression experiments identify kinetic controls on explosive silicic eruptions. Geophys. Res. Lett. 31, L08605.

Marxer, H., Bellucci, P., Nowak, M., 2015. Degassing of $H_2O$ in a phonolitic melt: a closer look at decompression experiments. J. Volcanol. Geotherm. Res. 297, 109–124.

Mastin, L.G., Ghiorso, M.S., 2000. A Numerical Program for Steady-State Flow of Magma-Gas Mixtures Through Vertical Eruptive Conduits. U.S.G.S. Open-File Report, 00-209.

Métrich, N., Bertagnini, A., Di Muro, A., 2010. Conditions of magma storage, degassing and ascent at Stromboli: new insights into the volcanic plumbing system with inferences on the eruptive dynamics. J. Petrol. 51, 603–626.
Miwa, T., Geshi, N., 2012. Decompression rate of magma at fragmentation: inference from broken crystals in pumice of vulcanian eruption. J. Volcanol. Geotherm. Res. 227-228, 76–84.
Mourtada-Bonnefoi, C.C., Laporte, D., 1999. Experimental study of homogeneous bubble nucleation in rhyolitic magmas. Geophys. Res. Lett. 26, 3505–3508.
Mourtada-Bonnefoi, C.C., Laporte, D., 2002. Homogeneous bubble nucleation in rhyoliticmagmas: an experimental study of the effect of $H_2O$ and $CO_2$. J. Geophys. Res. 107:B4. http://dx.doi.org/10.1029/2001JB00290.
Mourtada-Bonnefoi, C.C., Laporte, D., 2004. Kinetics of bubble nucleation in a rhyolitic melt: an experimental study of the effect of ascent rate. Earth Planet. Sci. Lett. 218, 521–537.
Mujin, M., Nakamura, M., 2014. A nanolite record of eruption style transition. Geology 42, 611–614.
Myers, M.L., Wallace, P.J., Wilson, C.J.N., Morter, B.K., Swallow, E.J., 2016. Prolonged ascent and episodic venting of discrete magma batches at the onset of the Huckleberry Ridge supereruption, Yellowstone. Earth Planet. Sci. Lett. 451, 285–297.
Navon, O., Lyakhovsky, V., 1998. Vesiculation processes in silicic magmas. Geol. Soc. London Spec. Pub. 145, 27–50.
Neri, A., Papale, P., Del Seppia, D., Santacroce, R., 2002. Coupled conduit and atmospheric dispersal dynamics of the AD Plinian eruption of Vesuvius. J. Volcanol. Geotherm. Res. 120, 141–160.
Ni, H., Zhang, Y., 2008. $H_2O$ diffusion models in rhyolitic melt with new high pressure data. Chem. Geol. 250:68–78. http://dx.doi.org/10.1016/j.chemgeo.2008.02.011.
Ni, H., Behrens, H., Zhang, Y., 2009. Water diffusion in dacitic melt. Geochim. Cosmochim. Acta 73:3642–3655. http://dx.doi.org/10.1016/j.gca.2009.03.029.
Nicholis, M.G., Rutherford, M.J., 2004. Experimental constraints on magma ascent rate for the crater flat volcanic zone hawaiite. Geology 32, 489–492.
Nowak, M., Cichy, S.B., Botcharnikov, R.E., Walker, N., Hurkuck, W., 2011. A new type of high-pressure low-flow metering valve for continuous decompression: first experimental results on degassing of rhyodacitic melts. Am. Mineral. 96, 1373–1380.
Ochs, F.A., Lange, R.A., 1999. The density of hydrous magmatic liquids. Science 283, 1314–1317.
Pallister, J.S., Hoblitt, R.P., Meeker, G.P., Knight, R.J., Siems, D.F., 1996. Magma mixing at Mount Pinatubo; petrographic and chemical evidence from the 1991 deposits. In: Newhall, C.G., Punongbayan, R.S. (Eds.), Fire and mud: Eruptions and lahars of Mount Pinatubo, Philippines. University of Washington Press, Seattle, pp. 687–731.
Papale, P., Dobran, F., 1993. Modeling of the ascent of magma during the Plinian eruption of Vesuvius in AD 79. J. Volcanol. Geotherm. Res. 58, 101–132.
Papale, P., Neri, A., Macedonio, G., 1998. The role of magma composition and water content in explosive eruptions – 1. Conduit ascent dynamics. J. Volcanol. Geotherm. Res. 87, 75–93.
Pardo, N., Cronin, S.J., Wright, H.M.N., Schipper, C.I., Smith, I., Stewart, B., 2014. Pyroclast textural variation as an indicator of eruption column steadiness in andesitic Plinian eruptions at Mt. Ruapehu. Bull. Volcanol. 76, 822.
Patzig, C., Hoche, T., Ditmer, M., Russel, C., 2012. Temporal evolution of crystallization in $MgO$-$Al_2O_3$-$SiO_2$-$ZrO_2$ glass ceramics. Cryst. Growth Des. 12, 2059–2067.
Pichavant, M., Di Carlo, I., Rotolo, S.G., Scaillet, B., Burgisser, A., Le Gall, N., Martel, C., 2013. Generation of $CO_2$-rich melts during basalt magma ascent and degassing. Contrib. Mineral. Petrol. 166, 545–561.
Preuss, O., Marxer, H., Ulmer, S., Wolf, J., Nowak, M., 2016. Degassing of hydrous trachytic Campi Flegrei and phonolitic Vesuvius melts: experimental limitations and chances to study homogeneous bubble nucleation. Am. Mineral. 101, 859–875.
Pupier, E., Duchenne, S., Toplis, M.J., 2008. Experimental quantification of plagioclase crystal size distribution during cooling of a basaltic liquid. Contrib. Mineral. Petrol. 155, 555–570.
Riello, P., Canto, P., Comelato, N., Polizzi, S., Verita, M., Hopfe, S., 2001. Nucleation and crystallization behavior of glass-ceramic materials in the $Li_2O$-$Al_2O_3$-$SiO_2$ system of interest for their transparency properties. J. Non-Cryst. Solids 288, 127–139.
Rust, A.C., Cashman, K.V., 2011. Permeability controls on expansion and size distributions of pyroclasts. J. Geophys. Res. 116:B11202. http://dx.doi.org/10.1029/2011jb008494.
Rutherford, M.J., 2008. Magma ascent rates. Rev. Mineral. 69, 241–271.
Rutherford, M.J., Hill, P.M., 1993. Magma ascent rates from amphibole breakdown: an experimental study applied to the 1980–1986 Mount St. Helens eruptions. J. Geophys. Res. 98 (19), 667–19,685.
Rutherford, M.J., Devine, J.D., 2003. Magmatic conditions and magma ascent as indicated by hornblende phase equilibria and reactions in the 1995–2002 Soufrière Hills magma. J. Petrol. 44, 1433–1453.
Sable, J.E., Houghton, B.F., Wilson, C.J.N., Carey, R.J., 2006. Complex proximal sedimentation from Plinian plumes: the example of Tarawera 1886. Bull. Volcanol. 69, 89–103.
Sable, J.E., Houghton, B.F., Wilson, C.J.N., Carey, R.J., 2009. Eruption mechanisms during the climax of the Tarawera 1886 basaltic Plinian eruption inferred from microtextural characteristics of the deposits. Geol. Soc. Lond. Spec. Publ. IAVCEI 2, 129–154.
Sahagian, D.L., Proussevitch, A.A., 1998. 3D particle size distributions from 2D observations: stereology for natural applications. J. Volcanol. Geotherm. Res. 84, 173–196.
Saltikov, S.A., 1967. The determination of the size distribution of particles in an opaque material from a measurement of the size distribution of their sections. In: Elias, H. (Ed.), Stereology. Springer-Verlag, NY, pp. 163–173.
Sato, H., 1995. Textural difference between pahoehoe and aa lavas of Izu-Oshima volcano, Japan: an experimental study on population density of plagioclase. J. Volcanol. Geotherm. Res. 66, 101–113.
Schlinger, C.M., Smith, R.M., 1986. Superparamagnetism in volcanic glasses of the KBS tuff: transmission electron microscopy and magnetic behavior. Geophys. Res. Lett. 13, 729–732.
Schlinger, C.M., Rosenbaum, J.G., Veblen, D.R., 1988. Fe-oxide microcrystals in welded tuff from southern Nevada: origin of remanence carriers by precipitation in volcanic glass. Geology 16, 556–559.
Schlinger, C.M., Veblen, D.R., Rosenbaum, J.G., 1991. Magnetism and magnetic mineralogy of ash flow tuffs from Yucca Mountain, Nevada. J. Geophys. Res. 96, 6035–6052.
Schmidt, B.C., Behrens, H., 2008. Water solubility in phonolite melts: influence of melt composition and temperature. Chem. Geol. 256, 258–267.
Schmidt, B.C., Blum-Oeste, N., Flagmeier, J., 2013. Water diffusion in phonolite melts. Geochim. Cosmochim. Acta 107, 220–230.
Sharp, T., Stevenson, R., Dingwell, D.B., 1996. Microlites and "nanolites" in rhyolitic glass: microstructural and chemical characterization. Bull. Volcanol. 57, 631–640.
Shea, T., Hammer, J.E., 2013. Kinetics of decompression and cooling-induced crystallization of mafic-intermediate hydrous magmas. J. Volcanol. Geotherm. Res. 260, 127–145.
Shea, T., Gurioli, L., Larsen, J.F., Houghton, B.F., Hammer, J.E., Cashman, K.V., 2010a. Linking experimental and natural vesicle textures in Vesuvius 79AD white pumice. J. Volcanol. Geotherm. Res. 192, 69–84.
Shea, T., Houghton, B.F., Gurioli, L., Cashman, K.V., Hammer, J.E., Hobden, B.V., 2010b. Textural analyses of vesicles in volcanic rocks: an integrated methodology. J. Volcanol. Geotherm. Res. 190, 271–289.
Shea, T., Gurioli, L., Houghton, B.F., Cioni, R., Cashman, K.V., 2011. Column collapse and generation of pyroclastic density currents during the A.D. 79 eruption of Vesuvius: the role of pyroclast density. Geology 39, 695–698.
Shea, T., Gurioli, L., Houghton, B.F., 2012. Transitions between fall phases and pyroclastic density currents during the AD 79 eruption at Vesuvius: building a transient conduit model from the textural and volatile record. Bull. Volcanol. 74, 2363–2381.
Shea, T., Hammer, J.E., First, E., 2013. Magma balloons or bombs? Nat. Geosci. 6, 802–803.
Shea, T., Leonhardi, T.C., Giachetti, T., Lindoo, A., Larsen, J.F., Sinton, J.H., Parsons, E., 2017. Dynamics of an unusual cone-building trachyte eruption at Pu'u Wa'awa'a, Hualālai volcano, Hawai'i. Bull. Volcanol. 79, 26.
Sigurdsson, H., Sparks, R., 1981. Petrology of rhyolitic and mixed magma ejecta from the 1875 eruption of Askja, Iceland. J. Petrol. 22, 41–84.
Sparks, R.S.J., Bursik, M.I., Carey, S.N., Gilbert, J.S., Glaze, L., Sigurdsson, H., Woods, A.W., 1997. Volcanic Plumes. John Wiley & Sons, p. 557.
Stewart, A.-M., Castro, J., 2016. P–T–X evolution of the 1280 AD Quilotoa dacite. J. Volcanol. Geotherm. Res. 313, 29–43.
Su, Y., Huber, C., 2017. The effect of non-linear decompression history on $H_2O/CO_2$ vesiculation in rhyolitic magmas. J. Geophys. Res. Solid Earth 122, 2712–2723.
Sutton, A.N., Blake, S., Wilson, C.J.N., 1995. An outline geochemistry of rhyolite eruptives from Taupo volcanic centre, New Zealand. J. Volcanol. Geotherm. Res. 68, 153–175.
Szramek, L.A., 2016. Mafic Plinian eruptions: is fast ascent required? J. Geophys. Res. 121. http://dx.doi.org/10.1002/2016JB013208.
Toramaru, A., 1989. Vesiculation process and bubble size distributions in ascending magmas with constant velocities. J. Geophys. Res. 94, 17523–17542.
Toramaru, A., 1995. Numerical study of nucleation and growth of bubbles in viscous magmas. J. Geophys. Res. 100, 1913–1931.
Toramaru, A., 2006. BND (bubble number density) decompression rate meter for explosive volcanic eruptions. J. Volcanol. Geotherm. Res. 154, 303–316.
Tuohy, R.M., Wallace, P.J., Loewen, M.W., Swanson, D.A., Kent, A.J.R., 2016. Magma transport and olivine crystallization depths in Kīlauea's east rift zone inferred from experimentally rehomogenized melt inclusions. Geochim. Cosmochim. Acta 185, 232–250.
Vetere, F., Iezzi, G., Behrens, H., Cavallo, A., Misiti, V., Dietrich, M., Knipping, J., Ventura, G., Mollo, S., 2013. Intrinsic solidification behaviour of basaltic to rhyolitic melts: a cooling rate experimental study. Chem. Geol. 354, 233–242.
Walker, D., Powell, M.A., Lofgren, G.E., Hays, J.F., 1978. Dynamic crystallization of a eucrite basalt. Proc. 9th Lunar Planet Sci. Conf. 1, 1369–1391.
Wallace, P.J., Anderson, A.T., 1998. Effects of eruption and lava drainback on the $H_2O$ contents of basaltic magmas at Kīlauea volcano. Bull. Volcanol. 59, 327–344.
Wehrmann, H., Bonadonna, C., Freundt, A., Houghton, B.F., Kutterolf, S., 2006. Fontana tephra: a basaltic plinian eruption in Nicaragua. Geol. Soc. Am. Spec. Pap. 412, 209–223.
Wilson, L., Head, J.W., 1981. Ascent and eruption of basaltic magma on the earth and moon. J. Geophys. Res. 86, 2971–3001.
Witter, J.B., Kress, V.C., Delmelle, P., Stix, J., 2004. Volatile degassing, petrology and magma dynamics of the Villarica lava lake, Southern Chile. J. Volcanol. Geotherm. Res. 134: 303–337. http://dx.doi.org/10.1016/j.jvolgeores.2004.03.002.
Worm, H.-U., Jackson, M., 1999. The superparamagnetism of Yucca Mountain tuff. J. Geophys. Res. 104, 25415–25425.
Zhang, Y., 1999. $H_2O$ in rhyolitic glasses and melts: measurement, speciation, solubility, and diffusion. Rev. Geophys. 37, 493–516.
Zhang, Y., Ni, H., 2010. Diffusion of H, C, and O components in silicate melts. Rev. Mineral. 72:171–225. http://dx.doi.org/10.2138/rmg.2010.72.5.
Zhang, Y., Xu, Z., Zhu, M., Wang, H., 2007. Silicate melt properties and volcanic eruptions. Rev. Geophys. 45, RG4004. http://dx.doi.org/10.1029/2006RG000216.